University of Iceland
Faculty of Natural Sciences
Department of Physics

RH-28-2010

*

Time-dependent transport

through a double quantum wire in a magnetic field

by

Nzar Rauf Abdullah

UNIVERSITY OF ICELAND

A thesis submitted in partial satisfaction
of the requirements for the degree of Master of
Science in Physics at the University of Iceland

*

Committee in charge:
Viðar Guðmundsson, Chair
Andrei Manolescu

Reykjavik
November 2010

Anyone who has never made a mistake
has never tried anything new
Albert Einstein

Abstract

We introduce a microscopic theory and a simulation method for time-dependent quantum transport through a finite size sample with interacting electrons connected to leads with non-interacting electrons via time-dependent coupling in an external magnetic field. The model is built on the *Quantum General Master Equation* (QGME) formalism that is used to investigate the time dependent current and the total many-electron charge distribution. We investigate interwire forward and backward scattering phenomena for a coupling element between the wires in a double wire sample. We observe that the electron-electron interaction delocalizes localized states in the system enhancing the electron transport.

Publication

The results reported here have been published in;

Time-dependent magnetotransport in an interacting double quantum wire with window coupling.
Nzar Rauf Abdullah, Chi-Shung Tang, and Vidar Gudmundsson.
Phys. Rev. B **82**, 195325 (2010).

Acknowledgments

The project is done as a partial requirement to complete MSc. at the Science Institute of the University of Iceland, under the supervision of Prof. Viðar Guðmundsson from the year 2009 to 2010.

First and foremost, I offer my sincerest gratitude to my supervisor Viðar Guðmundsson, whose encouragement, guidance and support from the initial to the final level enabled me to develop an understanding of the subject.

I would like to thank Prof. Andrei Manolescu for teaching me very interesting physics. Many thanks also to Prof. Chi-Shung Tang form the National United University in Taiwan for his helpful comments and a cooperation on publishing my results in Physical Review B.

I would also like to thank all people that have helped me during the study. These include all the members of the group and the members at the Science Institude.

A special thanks goes to Arann Taha Karim and his wife is Avan Anwar Faraj for helping me to stay in Iceland and introduce the Iceland culture to me during the study.

Lastly but not least, I offer my regards and blessings to my parents and sisters for their supports and love in any respect during the completion of the study.

The project was funded by the Icelandic Research Fund, and The Research Fund of the University of Iceland.

Contents

Abstract **i**

Publication **iii**

Acknowledgments **v**

List of Figures **ix**

1 Introduction **1**

1.1 Background Information 1

1.2 Fabrication of lateral double quantum wires 2

2 Model and Theory **5**

2.1 Quantum Transport 5

2.1.1 Single Electron Model 6

2.1.2 Many-Electron States And Coulomb Interaction 11

2.2 Quantum General Master Equation Formalism 14

2.3 Physical Measurable Quantities 16

3 Results And Simulation **19**

3.1 Parallel double wire system 20

3.2 Double wire with a single coupling-window 24

3.2.1 Effects of the magnetic field 27

3.2.2 Enhancement by the Coulomb interaction 32

3.2.3 The size influence of the coupling element 37

3.2.4 The nonlocal coupling geometry 41
3.3 Double wire with a double coupling-window elements 43

4 Summary and Conclusion **49**

A Single electron **51**
A.1 Central system 51
A.1.1 Single finite wire 51
A.1.2 Embedded finite wire 54
A.2 The Leads 58

B The many-electron eigenvalue problem **63**

C The QGME Formalism **65**

Bibliography **73**

List of Figures

1.1 Schematic diagram of a GaAs/AlGaAs heterostructure (a). Conduction band energy diagram (b), 2DEG appears at the GaAs/AlGaAs interface. 3

2.1 Schematic representation of an open quantum system. 5

2.2 Schematic energy states of the system. 11

3.1 (Color online) Schematic representation of the strength coupling in the contact regions for $B = 0$ T. $g_0^l a_w^{3/2} = 60$ meV, $\delta_x^l = \delta_y^l = 4.4 \times 10^{-4}$ nm^{-2}, and $a_w = 33.42$ nm. 20

3.2 (Color online) Schematic representation of the potentail defining the parallel double wire system. $B = 0$ T, $L_{\rm x} = 300$ nm, and $\hbar\Omega_0 = 1.0$ meV. 21

3.3 The noninteracting and interacting net current versus time for $B = 0.5$ T. 22

3.4 (Color online) The many-electron charge density for the noninteracting (left panel) and the interacting system (right panel). $B = 0.5$ T, $L_{\rm x} = 300$ nm. 23

3.5 (Color online) Schematic representation of the potential defining the window-coupled DW system. 3D plot (left panel) and contour plot (right panel). $B = 0$ T, $L_{\rm x} = 300$ nm, $L_{\rm w} = 100$ nm, and $\hbar\Omega_0 = 1.0$ meV. 24

3.6 (Color online) Energy spectrum of the leads (solid red) versus wave number q Fig.(a); and energy spectrum of the coupling window DW system (cross dot) versus the SES number n Fig.(b). $B = 0.5$ T, and the chemical potentials in the the leads are $\mu_L = 1.65$ meV and $\mu_R = 0.75$ meV (dashed green) such that $\Delta\mu = 0.9$ meV. The window of relevant states is defined by the dotted blue lines (1.5 meV). 25

3.7 The Energy spectrum of the twenty lowest single-electron states of the central system versus magnetic field. 27

3.8 The noninteracting net current versus time for various magnetic field, for a double quantum wire with a coupling element 28

3.9 The noninteracting net current versus time for various magnetic field, for a double quantum wire with a coupling element 29

3.10 The total charge of the noninteracting system, for a double quantum wire with a coupling element 30

3.11 (Color online) The many-electron charge density for the noninteracting system. $B = 0.0$ T (left), $B = 0.5$ T (middle) and $B = 1.0$ T (right). The system is a double wire with a coupling element 31

3.12 The noninteracting and the interacting left and right current for $B = 0.5$ T. 32

3.13 The noninteracting and the interacting net current for $B = 0.5$ T. 33

3.14 The total charge of the noninteracting (0) and interacting system (I). $B = 0.5$ T. 34

3.15 (Color online) The many-electron charge density for the noninteracting (left panel) and the interacting system (right panel). $B = 0.5$ T, $L_{\mathrm{x}} = 300$ nm, $L_{\mathrm{w}} = 100$ nm. 36

3.16 The non-interacting net current versus time for different size of the window , $B = 0.5$ T. 37

3.17 The interacting net current is plotted as a function of time for different size of the window, $B = 0.5$ T. 38

3.18 The interacting total charge versus time for different size of the window, $B = 0.5$ T. 39

3.19 (Color online) The interacting many-electron charge distribution with different size of the coupling window: $L_{\mathrm{w}} = 0.0$ nm (left), $L_{\mathrm{w}} = 50$ nm (middle), and $L_{\mathrm{w}} = 100$ nm (right). $B = 0.5$ T. . . . 40

3.20 The profile of the coupling strength in the y-direction. $B = 0.5$ T. 41

3.21 The interacting net current versus time for various nonlocal coupling strength. $B = 0.5$ T, $L_\mathrm{x} = 300$ nm, $L_\mathrm{w} = 100$ nm. 42
3.22 (Color online) The interacting many-electron charge distribution. Γ_1 (left), Γ_2 (middle) and Γ_3 (right). $B = 0.5$ T, $L_\mathrm{x} = 300$ nm, $L_\mathrm{w} = 100$ nm. 42
3.23 (Color online) Schematic representation of the potentail defining the parallel double wire with a double window-coupling system. $B = 0$ T, $L_\mathrm{x} = 300$ nm, $L_\mathrm{w} = 50$ nm, and $\hbar\Omega_0 = 1.0$ meV. . . . 43
3.24 The noninteracting and interacting net current versus time for $B = 1.0$ T. 44
3.25 The total charge of the noninteracting (0) and interacting system (I). $B = 1.0$ T. 45
3.26 (Color online) The many-electron charge density for the noninteracting (left panel) and the interacting system (right panel). $B = 1.0$ T, $L_\mathrm{x} = 300$ nm, and $L_\mathrm{w} = 50$ nm. 47

A.1 Schematic of the contour integration in the complex plane. . . . 61

Chapter 1

Introduction

1.1 Background Information

In the last three decades, the investigation of quantum transport in nanostructured semiconductors has been developed for various scientific reasons. The starting point to study semiconductor nanostructure was in the mid 1980s, when the size of physical structures had decreased towards the nanoscale. At that limit the quantum mechanical phenomena such as the discretization of energy levels becomes observable. When the electronic states are quantized, the electron-electron interactions is important. Finite nanostructures involve only few particles, whose interactions cannot be described by effective potentials, due to strong particle correlations. The single-particle picture most of the time breaks down and a full many-body method has to be used.

Many theoretical formalisms have been used to investigate time-dependent transport in nanoscale regime such as transfer Hamiltonian formalism [1], path integral technics [2], evolution operator method [3; 4], density functional theory (DFT) [5], Keldysh nonequilibrium Green function (NEGF) methods [6] and quantum master equations [7].

Our formalism here is the *Quantum General Master Equation* (QGME). Several approaches were introduced based on the master equation to study the time-dependent transport such as T-matrix formalism [8], time-convolutionless formalism [9], and super-operator formalism [10]. We use the super-operator formalism, which can be implemented either in the Markovian or without the Markovian approximation, [11–15].

Different approaches have been proposed based on the quantum master equation (QME) to study interaction effects in transport [16–18]. We use quantum general master equation without Markovian approximation to investigate the time-dependent transport properties including the electron-electron Coulomb interaction and on external perpendicular magnetic field in an open quantum system.

This formalism allows us to explore quantum interference features of the dynamical transient current. Quantum interference phenomena are important in a nanoscale electronic device. There are several systems developed for such studies, that may consist of parallel quantum dots [19], coupled quantum wires [20], side-coupled quantum dots [21; 22], two-path interferometers [23; 24], and Rashba double dots in a ring [25]. These coupled nanoscale systems have developed recent interest due to their potential applications as electronic spectroscopy tools [26], and in quantum information processing [27].

In this thesis, we will show how the magnetic field and the electron-electron (*e*-*e*) interaction affects the quantum transport and the interference features between the parallel quantum wires through a single or a double coupling window (we will define it in section 3.2) with a time-dependent coupling to the leads.

This thesis includes three more chapters in addition to this introduction chapter 1. In chapter 2, the main theoretical approaches and the formalism are introduced. We will show single and many electron models for describing the Hamiltonians of the three disconnected subsystems and the time-dependent contact Hamiltonians. Chapter 3 shows the main simulation results in this work. The conclusion and summary is included in the chapter 4.

1.2 Fabrication of lateral double quantum wires

Nano-scale device can be made to contain a layer of a high mobility *two-dimensional electron gas* (2DEG). It has been essential in investigating quantum transport because the Fermi-wavelength and the elastic scattering length can be larger than the dimensions of the device in the quantum regime.

The fabrication technic of double quantum wire can be divided into two main steps.

- Construction of a 2DEG in a semiconductor heterostructure.
- The dimensionality of the electron gas can be further reduced by several different micro and nano processing methods.

First Step There are many methods of fabricating a 2DEG in semiconductor nanostructures such as Molecular Beam Epitaxy-growth (MBE), Cleaved-edge overgrowth, Catalytic growth of nanowires and AFM lithography.

In MBE-growth the 2DEG can be fabricated at the interface between the GaAs substrate semiconductor and $Al_xGa_{1-x}As$ insulator layer (x is a fractional number which determines the concentration of Al) as seen in Fig. 1.1(a). The growth of an n-doped layer either as a single or a mixed $Al_xGa_{1-x}As$ layer provides electrons into the system. The second undoped AlGaAs layer interfaces with the GaAs cap, limiting the oxidation of AlGaAs.

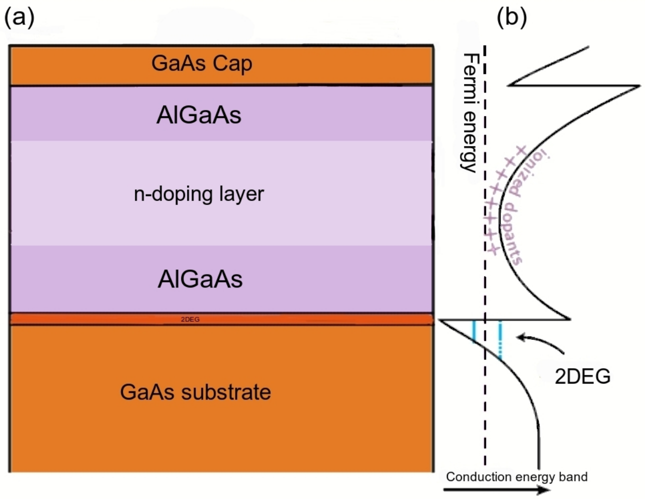

Figure 1.1: Schematic diagram of a GaAs/AlGaAs heterostructure (a). Conduction band energy diagram (b), 2DEG appears at the GaAs/AlGaAs interface.

In Fig. 1.1(b), the conduction band structure of the heterostructure is shown. It is clear that the band off-set of GaAs is smaller than that of $Al_xGa_{1-x}As$, but the two crystals have the same lattice structure.

The n-doped layer supplies the electrons into the GaAs layer. A triangular ‘quantum well’ is produced in the conduction band on the GaAs side. A thin layer of electrons is produced with low resistivity and high mobility the so-called 2DEG . The electrons can move freely parallel to the interface since the GaAs layer is undoped, but they are confined to the triangular well.

Second Step In the 2DEG a quantum wire can be fabricated by using negative gate voltage above the 2DEG. Two isolated conduction channels can be fabricated by a more complicated gate strip structure.

Chapter 2

Model and Theory

In this chapter we will take a tour of the theoretical part of time dependent transport through an open system. We introduce and explain various concepts and terms that will be referred to frequently in this thesis.

We begin with an overview of a single electron model in general, before introducing the methodology to describe the many-electron system. We will focus our concern on time evolution, and illustrate concepts such as the Quantum General Master Equation (QGME) formalism, for both non-interacting and interacting systems.

2.1 Quantum Transport

Our model that we investigate is an open quantum system composed of a mesoscopic sample connected to two electron reservoirs (leads) at the time moment $t = t_0$ via the contact region, but disconnected at earlier times. Our concern in this work is the time evolution of the open quantum system after $t > t_0$. The composite system consists of the left lead, right lead, and the sample in between,

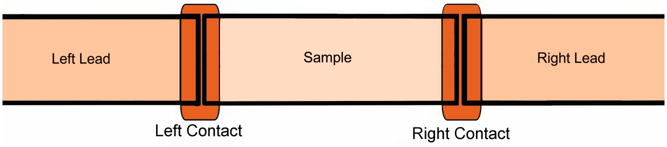

Figure 2.1: Schematic representation of an open quantum system.

which is shown in Fig. 2.1.

Electrons will be transferred from the leads into the sample via the contact regions (transfer regions) which are time dependent.

2.1.1 Single Electron Model

We will assume the system to be occupied by two-dimensional electrons that are hard-wall confined in the x-direction at $x = \pm L_x/2$ with L_x being the length of the sample and parabolically confined in the y-direction. The total Hamiltonian for the system consisting of the central system, leads, and a transfer Hamiltonian can be written as

$$h_{\text{System}}(t) = h_{\text{Sample}} + h_{\text{Leads}} + h_{\text{Transfer}}(t). \tag{2.1}$$

The first term describes the central system (sample), and the second term includes both left and right leads

$$h_{\text{Leads}} = \sum_{l=L,R} h_l, \tag{2.2}$$

where h_l is the Hamiltonian of the disconnected leads with l referring to the left (L) and right (R) leads. $h_{\text{Transfer}}(t)$ is time-dependent transfer Hamiltonian.

Central System (closed system for $t < t_0$)

The sample under investigation is composed of a laterally parallel double quantum wire, the time independent Hamiltonian is

$$h_{\text{Sample}} = h_{\text{S}} + V_{\text{DW}}. \tag{2.3}$$

h_{S} includes both the kinetic part and confining potential $V_{\text{conf}}(x,y) = V_{\text{h}}(x) + V_{\text{p}}(y)$. $V_{\text{h}}(x)$ denotes a hard-wall confining potential, $V_{\text{p}}(y)$ is the parabolic confinement, and V_{DW} is the potential describing the double quantum wire. If we apply a homogeneous magnetic field $\vec{B} = B\hat{z}$, choosing the vector potential in the Landau gauge $\vec{A} = -By\hat{x}$, then the Hamiltonian is

$$h_{\text{S}} = \frac{p_{\text{x}}^2}{2m^*} + \frac{p_{\text{y}}^2}{2m^*} + \frac{1}{2}m^*\Omega_w^2 y^2 + \omega_c y p_x, \tag{2.4}$$

here m^* is the effective mass of electrons in the GaAs, and $\Omega_w^2 = \Omega_0^2 + \omega_c^2$ is the effective cyclotron frequency, where Ω_0 denotes strength of the confinement potential, and $\omega_c = eB/m^*$ is the cyclotron frequency.

The eigenvalue equation for a single-electron in a disconnected sample in a magnetic field is

$$\left[\frac{p_{\mathrm{x}}^2}{2m^*}+\frac{p_{\mathrm{y}}^2}{2m^*}+\frac{1}{2}m^*\Omega_w^2y^2+\omega_c y p_x\right]\psi_n(x,y)=E_n\psi_n(x,y), \tag{2.5}$$

E_n are the eigenvalues of the central system and the index n refers to the quantum numbers $(n_x^{\mathrm{S}},n_y^{\mathrm{S}})$. The boundary condition of the wave functions (a) $\psi_n^{\mathrm{S}}(-\frac{L_x}{2},y)$ = $\psi_n^{\mathrm{S}}(\frac{L_x}{2},y)$ = 0 and (b) $\psi_n^{\mathrm{S}}(x,y\to\pm\infty)$ = 0, and Eq. (2.5) show us that the wave functions in general are not separable, but we can use an expansion in order to form the general solution

$$\Psi_n^{\mathrm{S}}=\sum_{n_x,n_y}C_{n_x}^{n_y}\varphi_{n_x}(x)\phi_{n_y}(y). \tag{2.6}$$

Where $\varphi_{n_x}(x)$ and $\phi_{n_y}(y)$ are complete basis wave functions with

$$\varphi_{n_x}(x)=\begin{cases}\sqrt{\dfrac{2}{L_x}}\cos\left(\dfrac{n_x\pi x}{L_x}\right) & n_x=1,3,5,...,\\[2ex] \sqrt{\dfrac{2}{L_x}}\sin\left(\dfrac{n_x\pi x}{L_x}\right) & n_x=2,4,6,...,\end{cases} \tag{2.7}$$

and

$$\phi_{n_y}(y)=\frac{\exp\left(-\dfrac{y^2}{2a_w^2}\right)}{\sqrt{2^{n_y}n_y!\sqrt{\pi}a_w}}\,\mathrm{H}_{n_y}(\frac{y}{a_w}). \tag{2.8}$$

H_{n_y} denotes the Hermit polynomial of order n_y and $a_w=\sqrt{\hbar/m^*\Omega_w}$ is an effective magnetic length. Using the basis wave functions to calculate the matrix elements of the Hamiltonian Eq. (2.4) the matrix elements of the non-perturbed Hamiltonian are

$$\langle n'|h_{\mathrm{S}}|n\rangle=\delta_{n_xn'_x}\delta_{n_yn'_y}\,\hbar\Omega_w\,\Xi^0_{n_x,n'_y}+\hbar\omega_c\,i\,a_wI_{n_x,n'_x}\,\Xi^{\mathrm{B}}_{n'_y,n_y}, \tag{2.9}$$

where,

$$\Xi^0_{n_x,n'_y}=\left[\frac{1}{2}\left(\frac{n_x\pi a_w}{L_x}\right)^2+\left(n'_y+\frac{1}{2}\right)\right],$$

$$\Xi^{\mathrm{B}}_{n'_y,n_y}=\left[\sqrt{\frac{n'_y}{2}}\delta_{n_y,n'_y-1}+\sqrt{\frac{n'_y+1}{2}}\delta_{n_y,n'_y+1}\right],$$

and

$$I_{n_x,n'_x} = \begin{cases} \dfrac{4n_x n'_x}{(n_x^2 - n'^2_x)L_x} \sin\left(\dfrac{n'_x\pi}{2}\right) \cos\left(\dfrac{n_x\pi}{2}\right), & \text{if } n_x = \text{even},\ n'_x = \text{odd}, \\ \\ \dfrac{4n_x n'_x}{(n_x^2 - n'^2_x)L_x} \sin\left(\dfrac{n_x\pi}{2}\right) \cos\left(\dfrac{n'_x\pi}{2}\right), & \text{if } n_x = \text{odd},\ n'_x = \text{even}. \end{cases}$$

The matrix element give the discrete eigenvalues of the sample with no embedded potential. The magnetic field in general can spread the eigenvalues or group them together. For derivation of further matrix elements see the appendix (A.1).

The Leads

We assume that the left and right leads are semi-infinite wires having the same y-confinement as the sample. The Hamiltonian of the leads can be written as

$$h_l = \frac{p_{\text{x}}^2}{2m^*} + \frac{p_{\text{y}}^2}{2m^*} + \frac{1}{2}m^*\Omega_w^2 y^2 + \omega_c y p_x, \tag{2.10}$$

but there is a different boundary condition here to solve the Schrödinger equation due to the range of the leads. The Schrödinger equation of a lead can be expressed in the following form

$$\left(\frac{p_{\text{x}}^2}{2m^*} + \frac{p_{\text{y}}^2}{2m^*} + \frac{1}{2}m^*\Omega_w^2 y^2 + \omega_c y p_x\right)\psi_{\mathbf{q}}^l(x,y) = E_{\mathbf{q}}\psi_{\mathbf{q}}^l(x,y), \tag{2.11}$$

where $E_{\mathbf{q}}$ are the eigenvalues of a lead with a quantum number $\mathbf{q}$ which denotes the continuous wave vector q and the subband index n_y^l. We use a simplified expression for the summation and integration $\int d\mathbf{q} \equiv \sum_{n_y}\int dq$. The boundary conditions are; (a) $\psi_{\mathbf{q}}^{\text{L}}(-\frac{L_x}{2},y) = 0$ and (b) $\psi_{\mathbf{q}}^{\text{L}}(x,y \longrightarrow \pm\infty) = 0$ for the left lead, and (a) $\psi_{\mathbf{q}}^{\text{R}}(\frac{L_x}{2},y) = 0$ and (b) $\psi_{\mathbf{q}}^{\text{R}}(x,y \longrightarrow \pm\infty) = 0$ for the right lead. Eq. (2.11) can not be solved using a separation of variables method, so we have to expand the wavefunctions as

$$\psi_{\mathbf{q}}^l(x,y) = \int d\mathbf{p}\, C^{n_y,n'_y}(q,p)\varphi_p^l(x)\phi_{n'_y}^l(y), \tag{2.12}$$

herein,

$$\varphi_p^l(x) = \frac{1}{\sqrt{2\pi}}\sin\left(p\left(x + \frac{L_x}{2}\right)\right), \tag{2.13}$$

and

$$\phi^{l}_{n'_y}(y) = \frac{\exp\left(-\frac{y^2}{2a_w^2}\right)}{\sqrt{2^{n'_y} n'_y! \sqrt{\pi} a_w}} \mathrm{H}_{n'_y}\left(\frac{y}{a_w}\right). \tag{2.14}$$

$\mathrm{H}_{n'_y}$ is the Hermit polynomial of order n'_y. Using the basis wave functions the matrix elements of a lead Hamiltonian in a magnetic field give us (see appendix A.2)

$$\sum_{n'_y} \left[\delta_{n_y,n'_y} \Upsilon^0_{q',n'_y} - \frac{\hbar\omega_c a_w}{4} q\, \Upsilon^B_{n_y,n'_y} \right] C^{n'_y,m_y}(q,p) = E_{p,m_y} C^{n_y,m_y}(q,p). \tag{2.15}$$

where

$$\Upsilon^0_{q',n'_y} = \hbar\Omega_{\mathrm{w}} \left[\frac{1}{2}\left(a_w q'\right)^2 + \left(n'_y + \frac{1}{2}\right) \right],$$

and

$$\Upsilon^B_{n_y,n'_y} = \sqrt{\frac{n'_y}{2}} \delta_{n_y,n'_y-1} + \sqrt{\frac{n'_y+1}{2}} \delta_{n_y,n'_y+1}.$$

The matrix elements look similar to the corresponding one for the finite wire (sample), except for the finite wire we ended up with a discrete eigenvalue problem, but here we have a continuous one represented by a homogeneous integral equation of the eigenvalue type.

Transfer Hamiltonian

In our system we have two time-dependent transfer Hamiltonians which make a connection between the sample and the left lead (h^L_T), and the sample and the right lead (h^R_T), so we can write the transfer Hamiltonian as $h_T(t) = h^L_T(t) + h^R_T(t)$. We start from a well-known single-particle transfer Hamiltonian in the spectral representation [28]

$$h^l_T(t) = \sum_n \int d\mathbf{q}\, \chi^l(t) \left(T^l_{\mathbf{q}n} |\psi^{\mathrm{S}}_n\rangle\langle\psi^l_{\mathbf{q}}| + \mathrm{h.c.} \right). \tag{2.16}$$

The coupling between eigenstates of the sample ψ^{S}_n and the leads $\psi^l_{\mathbf{q}}$ is described by the coefficients $T^l_{\mathbf{q}n}$ in the contacts. We express the time dependent coupling of the lead l by the switching-on function

$$\chi^l(t) = \theta(t-t_0) \left[1 - \frac{2}{e^{\gamma(t-t_0)}+1} \right], \tag{2.17}$$

where we have $\chi^L(t) = \chi^R(t)$ for $t > t_0$. The coupling between the central sample and the leads is switched on at $t = t_0$ and the parameter γ tells us the switching rate of the coupling. The coupling coefficients are defined as

$$T^l_{qn} = \int d\mathbf{r} d\mathbf{r}' \psi^l_{\mathbf{q}}(\mathbf{r}')^* g^l_{\mathbf{q}n}(\mathbf{r},\mathbf{r}') \psi^{\mathrm{S}}_n(\mathbf{r}). \tag{2.18}$$

The transfer of electrons between the single-electron states (SES) of the system $|n\rangle$ and the leads $|\mathbf{q}\rangle$ depends on the amplitude of the wave functions of the sample and the leads in the contact area. The nonlocal coupling function $g^l_{\mathbf{q}n}$ is given by

$$\begin{aligned} g^l_{\mathbf{q}n}(\mathbf{r},\mathbf{r}') &= g^l_0 \exp\left[-\delta^l_x(x-x')^2 - \delta^l_y(y-y')^2\right] \\ &\quad \times \exp\left(-|E_n - \varepsilon^l(\mathbf{q})|/\Delta_E\right). \end{aligned} \tag{2.19}$$

g^l_0 is the strength of the coupling, and Δ_E is a constant value. We have defined the energy interval $[\mu_R - \Delta, \mu_L + \Delta]$ to determine the active window that includes all the possible states in the central sample that may contribute to the transport. Basically all states below the active window are considered fully occupied and above it all states are empty, in addition there are no states below the active window in all our calculations. μ_L and μ_R are the chemical potential of the left and right lead respectively .

2.1.2 Many-Electron States And Coulomb Interaction

In order to include interaction between the electrons we resort here to a many electron formalism. The state of the system in Fock space is defined by a sequence of occupation numbers of the single particle states. The Many-Electron States (MES) are constructed from non-interacting SESs.

We denote non-interacting many-electron states of the isolated sample by $|\nu\rangle$. Note that only those SESs participate to transport that are located in the *relevant active window* $[\mu_R - \Delta, \mu_L + \Delta]$. Fig. 2.2 shows the possible states in the relevant active window.

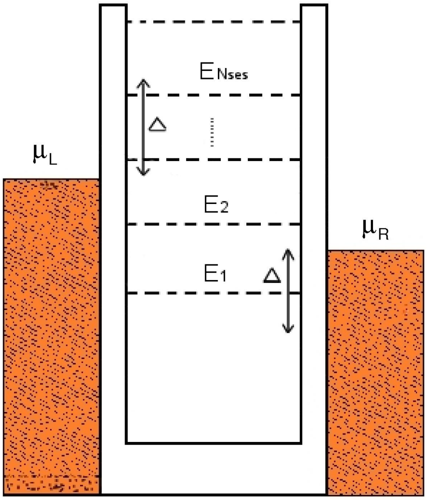

Figure 2.2: Schematic energy states of the system.

The single electron states in the active window are N_{SES}, so the many electron state are $N_{\text{MES}} = 2^{N_{\text{SES}}}$. In the occupation representation basis, the non-interacting MES can be written as

$$|\nu\rangle = |i_1^\nu, i_2^\nu, \ldots, i_n^\nu, \ldots, i_{N_{\text{SES}}}^\nu\rangle. \tag{2.20}$$

In our system we have fermions (electrons) so the occupation of the n-th SES of the isolated sample is $i_n^\nu = 0, 1$, empty state ($i_n^\nu = 0$), or occupied ($i_n^\nu = 1$).

In the many-electron description the Hamiltonian of the system will be presented as

$$H(t) = H_{\text{Sample}} + H_{\text{Leads}} + H_{\text{Transfer}}(t), \tag{2.21}$$

where the Hamiltonian of the central system is defined by

$$H_{\text{Sample}} = H_{\text{S}}^{0} + H_{\text{S}}^{I}. \tag{2.22}$$

H_{S}^{0} is the kinetic term and H_{S}^{I} is the Coulomb interaction term. The many-electron Hamiltonian of the leads consists of $H_{\text{Leads}} = \sum_{l=\text{L,R}} H_l$, and the time-dependent transfer Hamiltonian is $H_{\text{Transfer}}(t)$. We use capital letters here in order to distinguish from the single-electron form.

Hamiltonian of the central system

The electron-electron interaction plays a major role. According to the general rules of second quantization [29] and using the Fermi properties of the state vectors from Eq. (B.1) - Eq. (B.3) the kinetic term in the Hamiltonian is transformed into

$$H_{\text{S}}^{0} = \sum_{n} E_n d_n^{\dagger} d_n, \tag{2.23}$$

herein, E_n are the discrete single-electron energies, and $d_n^{\dagger}$ (d_n) have been introduced as the electron creation (annihilation) operators in the central system. We include the electron-electron Coulomb interaction in the central sample. Using the second quantization the Coulomb interaction is given by

$$H_{\text{S}}^{I} = \frac{1}{2} \sum_{n,m} \sum_{n',m'} V_{n,m;n',m'} d_n^{\dagger} d_m^{\dagger} d_{m'} d_{n'}. \tag{2.24}$$

The two-electron matrix elements are

$$V_{n,m;n',m'} = \langle nm|V|n'm'\rangle = \int d\mathbf{r} d\mathbf{r}' \psi_n^{\text{S}}(\mathbf{r})^{*} \psi_m^{\text{S}}(\mathbf{r}')^{*} V(\mathbf{r}-\mathbf{r}') \psi_{n'}^{\text{S}}(\mathbf{r}') \psi_{m'}^{\text{S}}(\mathbf{r}), \tag{2.25}$$

where $\psi_i^{\text{S}}(\mathbf{r})$ are the single-electron wavefunctions of the sample. The Coulomb kernel is

$$V(\mathbf{r}-\mathbf{r}') = \frac{e^2}{4\pi\varepsilon_0\varepsilon_r} \frac{1}{\sqrt{(x-x')^2 + (y-y')^2 + \eta^2}}, \tag{2.26}$$

with the relative dielectric constant of the material ε_r, and η an infinitesimal convergence parameter. The MES Hamiltonian of the central sample Eq. (2.22) is transformed to the following form

$$H_{\text{Sample}} = \sum_n E_n d_n^\dagger d_n + \frac{1}{2} \sum_{n,m} \sum_{n',m'} V_{n,m;n',m'} d_n^\dagger d_m^\dagger d_{m'} d_{n'}. \qquad (2.27)$$

The Coulomb interacting MES of the isolated central system are derived with the *exact diagonalization* method [30]. The energy corresponding to the non-interacting MES is denoted by $\mathscr{E}^0_{\nu'\nu} = \sum_n E_n i_n^\nu$ which is the sum of the occupied single-electron states.

Hamiltonian of a lead

We introduce the electron creation $c_{\mathbf{q}}^\dagger$ and annihilation operators $c_{\mathbf{q}}$ of a lead associated to the respective SES. The many-electron Hamiltonian of a lead can be expressed in the following form

$$H_{\text{Leads}} = \sum_{l=\text{L,R}} \int d\mathbf{q}\, \varepsilon^l(\mathbf{q}) c_{\mathbf{q}}^{l\,\dagger} c_{\mathbf{q}}^l. \qquad (2.28)$$

$\varepsilon^l(\mathbf{q})$ is the energy spectrum of a lead. Note that the *e*-*e* interaction in the leads is neglected.

Transfer Hamiltonian

In the previous discussion we have introduced the transfer Hamiltonian in the SES basis. Now in the MES basis, using the creation $d_n^\dagger$ and annihilation d_n operators of the central sample, and the creation $c_{\mathbf{q}}^{l\,\dagger}$ and annihilation $c_{\mathbf{q}}^l$ operators of a lead, the time-dependent transfer Hamiltonain in the third term of Eq. (2.21) is expressed as

$$H_{\text{Transfer}}(t) = \sum_{l=\text{L,R}} \chi^l(t) \sum_n \int d\mathbf{q} \left[c_{\mathbf{q}}^{l\,\dagger} T_{\mathbf{q}n}^l d_n + d_n^\dagger (T_{n\mathbf{q}}^l)^* c_{\mathbf{q}}^l \right]. \qquad (2.29)$$

The first term can be explained as a creation of an electron in the lead and the annihilation of an electron in the sample. The second term gives us the annihilation of an electron in a lead and a creation of an electron in the sample i.e. an electron is transferred from the lead l to the sample.

2.2 Quantum General Master Equation Formalism

In this section we will discuss the dynamics of open systems (S) under the influence of the reservoirs (R), or the leads (l). The dynamical behavior of a system can generally be described by the so-called Quantum Generalized Master Equation. Master equations were first introduced by Pauli [31] in quantum statistical mechanics. He assumed that the expansion coefficient of the wavefunction have random phases at all times. This gives a dynamical behavior in terms of occupation numbers of the wavefunction. Later Nakajima in 1958 [32] and Zwanzig in 1960 [33] independently proved that this assumption of continuously random phase is unnecessary.

Our starting point is the equation of motion for the full density operator. For the composite system S$\oplus$R, the time evolution of the density operator for the whole (full) system is described by the Liouville-von Neumann (quantum Liouville) equation [34]

$$\frac{d\rho(t)}{dt} = -\frac{i}{\hbar}\left[H(t),\rho(t)\right]. \tag{2.30}$$

$\rho(t)$ is the *full* density operator. Our approach to derive an equation of motion for the reduced density matrix ρ_{S} of the central system is the super-operator method in line with the Nakajima-Zwanzig method. In this method the full density operator is projected into two parts as

$$\rho(t) = \mathscr{P}\rho(t) + Q\rho(t), \tag{2.31}$$

where the first term is said to be the *relevant* and the second term is the *irrelevant* part of the density ρ of the full system. The aim here is to derive the equation of motion for the relevant part $\mathscr{P}\rho(t)$. We define the super-operator as $\mathscr{P} = \rho_l \mathrm{Tr}_{\mathrm{Leads}}$ and the complementary super-operator $Q = 1 - \mathscr{P}$. We wish to find the reduced density operator (RDO) of the central system ρ_{S}, that can be obtained by taking the trace over the Fock space of the leads

$$\rho_{\mathrm{S}}(t) = \mathrm{Tr}_{\mathrm{Leads}}(\mathscr{P}\rho(t)), \tag{2.32}$$

with the initial conditions $\rho(t<t_0) = \rho_{\mathrm{L}}\rho_{\mathrm{R}}\rho_{\mathrm{S}}^{0}$, where ρ_{S}^{0} is the density operator of the isolated sample at $(t<t_0)$. At that time we can assume that the sample is unoccupied

$$\rho_{\mathrm{S}}^{0} = |\nu_0\rangle\langle\nu_0|, \qquad |\nu_0\rangle = |0,0,\ldots,i^{\nu}_{N_{\mathrm{SES}}} = 0,\ldots\rangle, \tag{2.33}$$

we also assume that at $t < t_0$ the leads are in thermal equilibrium, so the density matrix for the leads ρ_l is then given by

$$\rho_l = \frac{e^{-\beta(H_l - \mu_l N_l)}}{\mathrm{Tr}_l\{e^{-\beta(H_l - \mu_l N_l)}\}}. \tag{2.34}$$

μ_l is the chemical potential of the lead and N_l denotes the number operator of the lead l. The chemical potential gives us the distribution of electrons in the leads. Using the initial conditions we end up with the following non-interacting QGME for the RDO

$$\frac{d\rho_{\mathrm{S}}(t)}{dt} = -\frac{i}{\hbar}\left[H_{\mathrm{Sample}}, \rho_{\mathrm{S}}(t)\right] - \frac{1}{\hbar^2}\sum_{l=L,R}\chi^l(t)\int d\mathbf{q}\left(\left[\mathscr{T}^l(\mathbf{q}), \Omega^l_{\mathbf{q}}(t)\right] + \mathrm{h.c.}\right), \tag{2.35}$$

an integro-differential equation. The kernel of the equation is approximated in H_{T} up to second order

$$\Omega^l_{\mathbf{q}}(t) = U^\dagger_{\mathrm{S}}(t)\int_{t_0}^{t} dt'\,\chi^l(t')\Pi^l_{\mathbf{q}}(t') \times\ e^{\left(-\frac{i}{\hbar}(t-t')\varepsilon^l(\mathbf{q})\right)}U_{\mathrm{S}}(t),$$

and

$$\Pi^l_q(t') = U_{\mathrm{S}}(t')\left[\left(\mathscr{T}^l(\mathbf{q})\right)^\dagger\rho_{\mathrm{S}}(t')\left(1 - f^l\left(\varepsilon(\mathbf{q})\right)\right) - \rho_{\mathrm{S}}(t')\left(\mathscr{T}^l(\mathbf{q})\right)^\dagger f^l\left(\varepsilon(\mathbf{q})\right)\right]U^\dagger_{\mathrm{S}}(t').$$

$U_{\mathrm{S}}(t) = e^{iH_{\mathrm{Sample}}t/\hbar}$ denotes the time evolution operator of the closed central system and $f^l\left(\varepsilon(\mathbf{q})\right)$ is the Fermi distribution in the lead l before coupling. To see the details of the derivation please refere to appendix (C).

We use the exact diagonalization method to supply a new interacting MES basis $|\mu)$ including all sectors in Fock space containing from 0 to N_{SES} electrons. The many-electron basis are connected by a unitary transformation

$$|\mu) = \sum_\nu \mathscr{U}_{\mu\nu}|\nu\rangle, \tag{2.36}$$

with the transformation matrix $\mathscr{U}_{\mu\nu}$. Given the unitary transformation one can transform the equation for the non-interacting RDO into the equation for interacting RDO. The non-interacting many-electron coupling matrix is transformed to the interacting case $\widetilde{\mathscr{T}^l}(\mathbf{q}) = \mathscr{U}^\dagger\mathscr{T}^l(\mathbf{q})\mathscr{U}$. Expressing the interacting many-electron coupling matrix $\widetilde{\mathscr{T}}$ in the interacting MES

$$\widetilde{\mathscr{T}^l}(\mathbf{q}) = \sum_{\mu,\mu'}\widetilde{\mathscr{T}^l_{\mu\mu'}}(\mathbf{q})|\mu)(\mu'|, \tag{2.37}$$

with $\widetilde{\mathscr{T}}^l_{\mu\mu'}(\mathbf{q}) = \sum_n T^l_{n\mathbf{q}}(\mu|d_n^\dagger|\mu')$ in terms of the single-electron coupling matrix $T^l_{n\mathbf{q}}$.

Substituting the diagonalized matrix representation of the interacting H_{Sample} allows us to obtain the RDO in the interacting MES basis $\widetilde{\rho}_{\text{S}} = \mathscr{U}^\dagger \rho_{\text{S}} \mathscr{U}$. The QGME is transformed to

$$\frac{d\widetilde{\rho}_{\text{S}}(t)}{dt} = -\frac{i}{\hbar}\left[\widetilde{H}_{\text{Sample}}, \widetilde{\rho}_{\text{S}}(t)\right] - \frac{1}{\hbar^2}\sum_{l=L,R}\chi^l(t)\int d\mathbf{q}\left(\left[\widetilde{\mathscr{T}}^l(\mathbf{q}), \widetilde{\Omega}^l_{\mathbf{q}}(t)\right] + \text{h.c.}\right), \tag{2.38}$$

where the kernel is constructed from

$$\widetilde{\Omega}^l_{\mathbf{q}}(t) = U_{\text{S}}^\dagger(t)\int_{t_0}^{t} dt'\,\chi^l(t')\widetilde{\Pi}^l_{\mathbf{q}}(t') \times e^{\left(-\frac{i}{\hbar}(t-t')\varepsilon^l(\mathbf{q})\right)} U_{\text{S}}(t),$$

with

$$\widetilde{\Pi}^l_{\mathbf{q}}(t') = U_{\text{S}}(t')\left[\left(\widetilde{\mathscr{T}}^l\right)^\dagger \widetilde{\rho}_{\text{S}}(t')\left[1 - f^l\left(\varepsilon(\mathbf{q})\right)\right] - \widetilde{\rho}_{\text{S}}(t')\left(\widetilde{\mathscr{T}}^l\right)^\dagger f^l\left(\varepsilon(\mathbf{q})\right)\right] U_{\text{S}}^\dagger(t').$$

Eq. (2.38) is the main equation of this work. The first term gives the evolution of the disconnected but interacting sample. The second term allows for charging and discharging processes. Electrons in a given state of the sample n are allowed to transfer out in a state $\mathbf{q}$ of the lead at a specific time and transfer back in a different state at the same time or different time. We should note the reduced density operator is nonlocal in time pointing to non-Markovian memory effects.

2.3 Physical Measurable Quantities

The RDO allows us to compute physical quantities such as time evolution of the charge, many-electron charge distribution and the net current. Note that all these quantities defined below will be in the interacting MES basis.

Evolution of the charge density

The charge operator is described as

$$\hat{Q}_{\text{S}} = e\sum_n d_n^\dagger d_n. \tag{2.39}$$

The statistical time evolution of the charge operator is

$$\langle \hat{Q}_{\text{S}}(t)\rangle = \text{Tr}\{\widetilde{\rho}(t)\hat{Q}_{\text{S}}\}, \tag{2.40}$$

with the trace over the Fock space $\mathrm{Tr} = \mathrm{Tr}_\mathrm{S}\mathrm{Tr}_\mathrm{Leads}$. Using $\rho_\mathrm{S}(t) = \mathrm{Tr}_\mathrm{Leads}\ \rho(t)$, and convert the RDO $\rho_\mathrm{S}(t)$ from noninteracting MES basis to the interacting MES basis, the average charge evolution becomes

$$\begin{aligned}\langle \hat{Q}_\mathrm{S}(t)\rangle &= \mathrm{Tr}_\mathrm{S}\{\widetilde{\rho}_\mathrm{S}(t)\hat{Q}_\mathrm{S}\} \\ &= e\sum_n\sum_\mu (\mu|\widetilde{\rho}_\mathrm{S}(t)\ d_n^\dagger d_n|\mu).\end{aligned} \tag{2.41}$$

It is clear that the time-dependent charge is related to the diagonal elements of the RDO.

Net current

Having the time evolution of the mean value of the charge operator one can introduce the time-dependent net current from the left to right leads through the sample, so-called *net charge current*

$$I_\mathrm{Q}(t) = \frac{d\langle \hat{Q}_\mathrm{S}(t)\rangle}{dt} = I_\mathrm{L}(t) - I_\mathrm{R}(t) = e\sum_n\sum_{\mu\mu'}\frac{d\widetilde{\rho}_{\mathrm{S};\mu\mu'}}{dt}(\mu'|d_n^\dagger d_n|\mu). \tag{2.42}$$

Charging processes occur if electrons flow from the left or the right lead towards the sample and we have discharging processes if the electrons flow from the sample towards the left or the right lead.
We see the net current depends on the time derivation of the reduced density matrix. One can write,

$$\frac{d\widetilde{\rho}_{\mathrm{S};\mu\mu'}}{dt} = -\frac{\chi^l(t)}{\hbar^2}\int d\mathbf{q}\ \left(\mu\left|\left(\left[\widetilde{\mathscr{T}}^l(\mathbf{q}),\widetilde{\Omega}^l_\mathbf{q}(t)\right]+\mathrm{h.c.}\right)\right|\mu'\right). \tag{2.43}$$

we should note that the first term vanished since it is a trace of a commutator.

Electron charge distribution

The last interesting physical parameter to calculate in our work is the many electron charge distribution. One can explicity write

$$Q(\mathbf{r},t) = e\sum_{n',n}\psi^*_{n'}(\mathbf{r})\psi_n(\mathbf{r})\sum_{\mu,\mu'}\widetilde{\rho}_{\mathrm{S};\mu\mu'}(t)(\mu|d^\dagger_{n'}d_n|\mu'). \tag{2.44}$$

The many electron charge distribution depends both on space and time.

Chapter 3

Results And Simulation

In this chapter we will show the main results we have obtained in this work. We will focus on the time-dependent transport properties and the quantum interference behavior between the parallel wires in the case when they have a coupling element between them.

Since electrons in a nanostructure are generally sensitive to magnetic field, we are using a natural length scale of the system, the effective magnetic length a_w to characterize the x and y axis. The influence of the magnetic field on the effective magnetic length is determined by the following

$$\begin{aligned} a_w &= \left(\frac{\hbar}{m^*\Omega_0}\right)^{1/2}\left(\frac{1}{1+(eB/(m^*\Omega_0))^2}\right)^{1/4} \\ &= \frac{33.74}{\sqrt[4]{1+2.982[B(\mathrm{T})]^2}}\ \mathrm{nm}. \end{aligned} \tag{3.1}$$

The electron effective mass $m^* = 0.067m_e$ for a *GaAs* semiconductor which we have assumed the wires are made of. It is clear that the effective magnetic length is proportional to the inverse square root of the magnetic field in the case of large field.

In addition, we should write the main physical parameters that we use in all simulations as constant values independent of the magnetic field.

- To control a thermal motion of electron in our system, the temperature $T = 0.5$K is used.
- The states of the central system within the bias are completely unoccupied before switching-on the coupling.

- The confinement potential of the central system and the leads are equivalent to the confinement frequency $\hbar\Omega_0 = \hbar\Omega_l = 1.0$ meV, which is shown in Fig. 2.1.

- The coupling parameter which controls the transport is the nonlocal coupling strength $\Gamma^l = 4g_0^l a_w^{3/2}/(\delta_x^l \delta_y^l)^{1/2}$ determining the strength of the coupling between the central sample and the leads. In all calculations the contact size parameters are $\delta_x^l = \delta_y^l = 4.4 \times 10^{-4}$ nm^{-2} and $g_0^l a_w^{3/2} = 60$ meV such that the coupling strength $\Gamma^l = 54.5$ meV·nm^2. Using these parameters one can determine the effective lengths of the system-lead coupling potential which are $L_{c,x}^l = L_{c,y}^l \approx 95$ nm. Fig. 3.1 shows the nonlocal coupling function Eq. (2.19) in the contact regions.

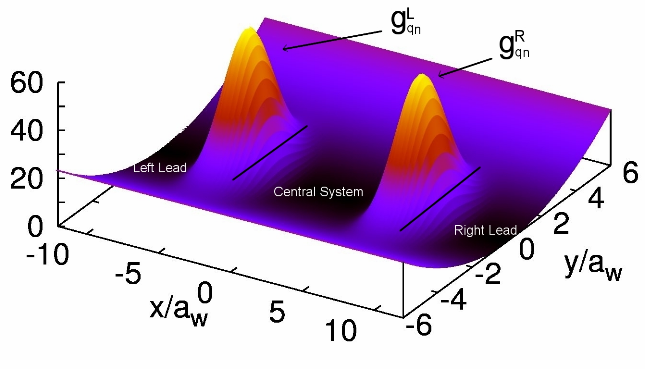

Figure 3.1: (Color online) Schematic representation of the strength coupling in the contact regions for $B = 0$ T. $g_0^l a_w^{3/2} = 60$ meV, $\delta_x^l = \delta_y^l = 4.4 \times 10^{-4}$ nm^{-2}, and $a_w = 33.42$ nm.

3.1 Parallel double wire system

We start with parallel laterally double quantum wires of length L_x, which are separated by the barrier potential, and the electrons of both wires are in tunneling contact through the central barrier. The potential has this form

$$V_{\mathrm{MB}}(y) = V_B\, e^{(-\beta^2 (y-y_0)^2)}. \tag{3.2}$$

In Fig. 3.2 the double wire system is demonstrated, where the constant parameters have the following values

$$V_B = 18\ \text{meV} \qquad \beta = 0.3\ \text{nm}^{-1}, \qquad y_0 = 0\ a_w.$$

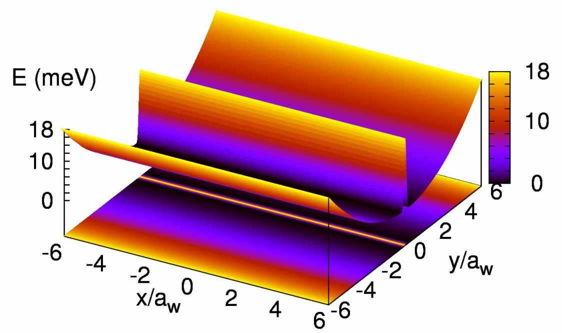

Figure 3.2: (Color online) Schematic representation of the potentail defining the parallel double wire system. $B = 0$ T, $L_x = 300$ nm, and $\hbar\Omega_0 = 1.0$ meV.

We assume that the chemical potentials $\mu_L = 1.65$ meV and $\mu_R = 0.75$ meV are fixed. This provides a constant bias window $\mu_L - \mu_R = -eV_{\text{bias}} = 0.9$ meV. The extention parameter ($\Delta = 0.3$ meV) which is the extended bias window to give the window of relevant states $\Delta\mu + 2\Delta = 1.5$ meV

We consider five single-electron states in the relevant bias window and distributed as follows: three states are located in the active bias window $[\mu_L, \mu_R]$, two other states are located in the top extended bias window $[\mu_L, \mu_L + \Delta]$. One subband in the leads is located in the relevant bias window (not shown).

The time-dependent current for the double nanowires is calculated. It is presented in Fig. 3.3, where $I_{L,0}$ is the noninteracting current flowing from the left lead into the central system, $I_{R,0}$ is the noninteracting current flowing from the sample to the right lead, the noninteracting net current $I_{Q,0}$, and the interacting net current $I_{Q,I}$, where the net current $I_Q = I_L - I_R$.

We present here the total left and right current to see how the current tunnels from both leads into or out of the sample. When we switch-on the coupling at $t = t_0$, the left current is increasing with time up to $t = 35$ ps with having rapid oscillation, while the right current has a small fluctuation at the beginning. Later on, both the left and right current are approaching to the steady states with small oscillations.

Now we look at the net current for the noninteracting and interacting system, both of them are increasing with time and almost having the same value up to $t = 30$ ps. Then the net current is exponentially decreasing with time at time $t = 140$ ps the difference between noninteracting and interacting current becomes 0.1 nA (The Coulomb correlation $\sim$ 10%).

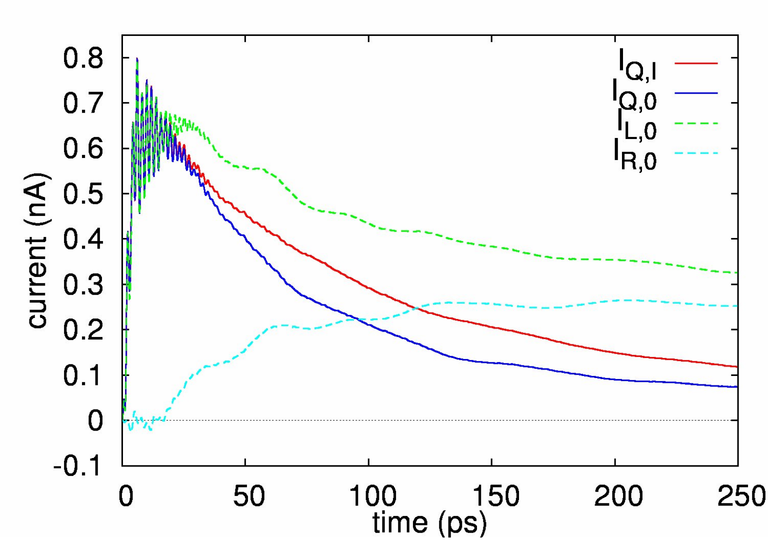

Figure 3.3: The noninteracting and interacting net current versus time for $B = 0.5$ T.

To see the behavior of the charge motion, we will show the many-electron charge distribution in the central system. Fig. 3.4 displays the noninteracting (left panel) and interacting (right panel) many-electron charge distribution for four selected moment of time during the transient current. At time $t = 10$ ps, it indicates a motion of electrons from the left side to the right side, while for $t = 20$ ps the charge density is moving from the right side to the left side of the central sample, i.e. at short time regime we have oscillations in the charge motion in accordance with the oscillation behavior in the current. Note that the Coulomb interaction does not have a great influence on the charge motion at this initial.

Later on, at time $t = 120$ ps the many-electron charge motion has small oscillations and the Coulomb interaction enhances the current that is clearly carried by both wires. The central system is approaching to the steady state at $t = 220$ ps and the Coulomb interaction continues to it's enhancement of the current.

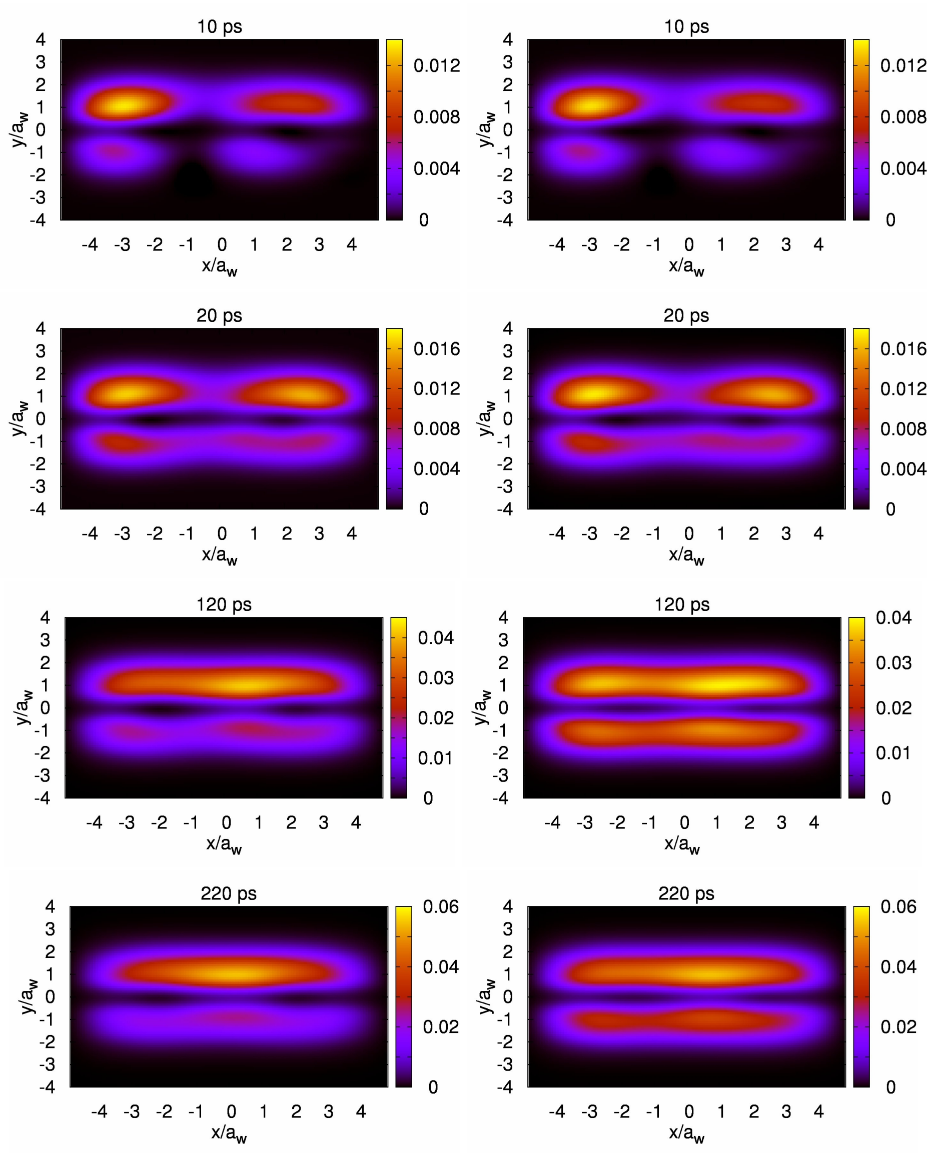
10 ps

10 ps

20 ps

20 ps

120 ps

120 ps

220 ps

220 ps

Figure 3.4: (Color online) The many-electron charge density for the noninteracting (left panel) and the interacting system (right panel). $B = 0.5$ T, $L_x = 300$ nm.

3.2 Double wire with a single coupling-window

The geometrical shape of the sample is designed as a lateral double nanowire of length L_x. The electron systems of both wires are in tunneling contact through the central barrier and the contacts. To further observe interference phenomena and interwires transfers, we put coupling elements in the barrier between the nanowires. The coupling elements are windows in the potential barrier separating the wires. The wires have the same confinement potential and the same length. The potential defining the double wire (DW) subsystem with a coupling element is described by

$$V_{\mathrm{DW}}(\mathbf{r}) = V_{\mathrm{MB}}(y) + V_{\mathrm{CW}}(x,y), \tag{3.3}$$

where V_{MB} is the middle barrier potential which separates the quantum wires and V_{CW} is the potential of the coupling window, a Gaussian potential has been chosen in both cases

$$V_{\mathrm{MB}}(y) = V_B\, e^{(-\beta^2(y-y_0)^2)}, \tag{3.4}$$

$$V_{\mathrm{CW}}(x,y) = -V_W\, e^{(-\beta_x^2(x-x_1)^2-\beta_y^2(y-y_1)^2)}. \tag{3.5}$$

Where V_B and V_W are the respective potential strengths. $(x_i,\ y_i)$ are the center coordinates of the window between the wires, β, β_x and β_y determine the range of the potential.

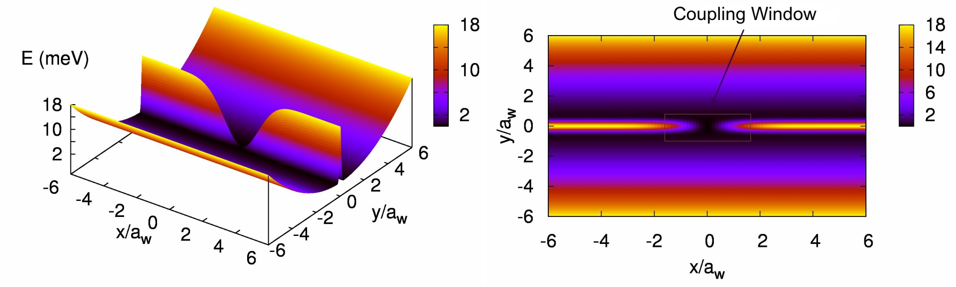

Figure 3.5: (Color online) Schematic representation of the potential defining the window-coupled DW system. 3D plot (left panel) and contour plot (right panel). $B = 0$ T, $L_{\mathrm{x}} = 300$ nm, $L_{\mathrm{w}} = 100$ nm, and $\hbar\Omega_0 = 1.0$ meV.

Fig. 3.5 illustrates the double nanowires with a window-coupled system, the parameters are,

- $V_B = 18$ meV, $\beta = 0.3$ nm^{-1}, $y_0 = 0\ a_w$
- $V_W = 18$ meV, $\beta_x = 0.02$ nm^{-1}, $\beta_y = 0.3$ nm^{-1}, $x_1 = y_1 = 0\ a_w$.

In all our calculation we will fix the bias voltage of the system. Given the bias window one can determine how many single electron states are in the central system and how many energy subbands in the leads are needed to describe the transport. We assume that the chemical potential in the left lead $\mu_R = 1.65$ meV and the chemical potential in the right lead $\mu_R = 0.75$ meV are fixed. This gives us a constant bias window $\Delta\mu = \mu_L - \mu_R = -eV_{\text{bias}} = 0.9$ meV. The extention parameter ($\Delta = 0.3$ meV) which is the extended bias window to give the window of relevant states $\Delta\mu + 2\Delta = 1.5$ meV. Shown in the Fig. 3.6.

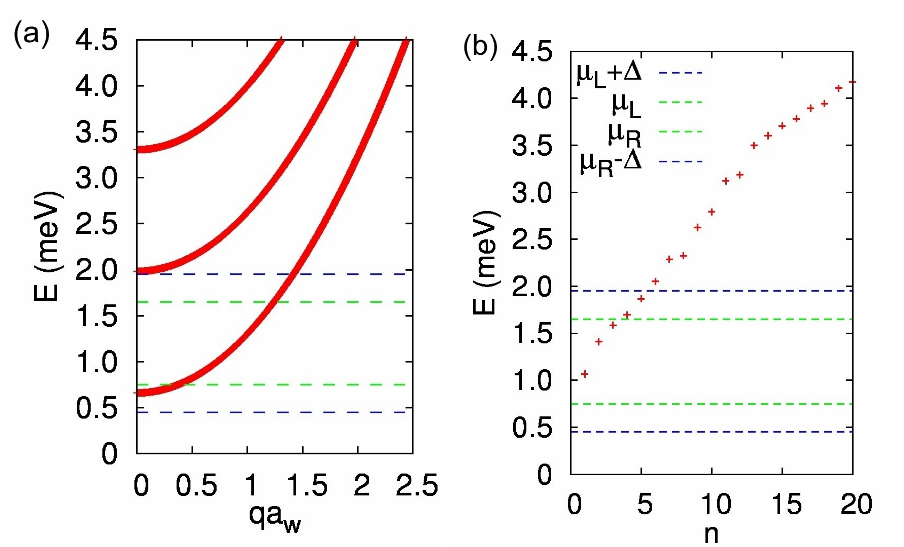

Figure 3.6: (Color online) Energy spectrum of the leads (solid red) versus wave number q Fig.(a); and energy spectrum of the coupling window DW system (cross dot) versus the SES number n Fig.(b). $B = 0.5$ T, and the chemical potentials in the the leads are $\mu_L = 1.65$ meV and $\mu_R = 0.75$ meV (dashed green) such that $\Delta\mu = 0.9$ meV. The window of relevant states is defined by the dotted blue lines (1.5 meV).

The energy spectrum of the leads as a function of wave number q scaled by a_w^{-1} is presented in the Fig. 3.6(a). We see that the first subband is the most important subband in the leads since the bias window $\Delta\mu$ is located in it. Further more, the top of the relevant (extended) active bias window covers the threshold of the second subband and the bottom of the relevant active bias window covers the evanescent modes below the first subband.

The discrete energy levels as a function of the single electron quantum number n of the central sample is shown in the Fig. 3.6(b), the window of the relevant states contains five single electron states (SESs), such that three SESs are located in the bias window while the other two SESs are located in the top of the extended bias window. We should note that the length and the effective width of the double nanowire does influence the contribution of single-electron states to the bias window.

The main focuses here is on the time-depending transport properties and the interference behavior between the wires in the presense of the coupling elements in the barrier between the wires. We will show the influences of following parameters on the transport: the magnetic field, the Coulomb interaction, the coupling window size, and the geometric of the nonlocal coupling function.

3.2.1 Effects of the magnetic field

Now we discuss the influence of the magnetic field on the current dynamics. The energy spectrum has an important role in the transport behavior. In Fig. 3.7 the energy spectrum of the twenty lowest states of the central system as a function of the magnetic field is plotted. We can generally see that the energy spectrum rises with increasing magnetic field. The difference between the ground state $n = 1$ and the first excited state $n = 2$ energy is ~ 0.49 meV for $B = 0.0$ T, when the magnetic field increases to $B = 1.0$ T the difference becomes ~ 0.16 meV. One can see clearly how the states tend to group together in higher magnetic field. This leads to a change of the single electron states in the bias window.

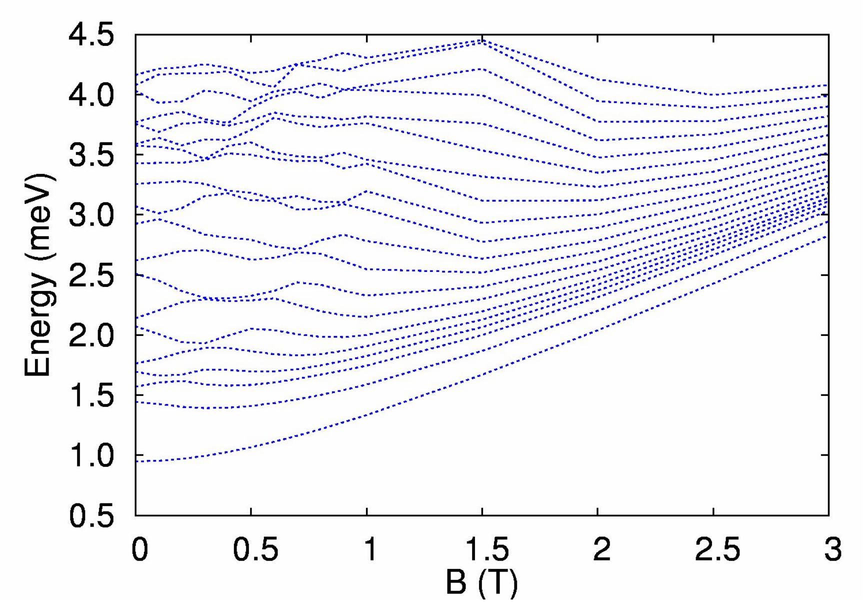

Figure 3.7: The Energy spectrum of the twenty lowest single-electron states of the central system versus magnetic field.

Now let's observe the time-dependent behavior of the current for different magnetic fields in the non-interacting system. We have mentioned that the physical parameters $g_0^l a_w^{3/2}$, $\delta_x^l a_w^2$, and $\delta_y^l a_w^2$ are fixed during our all calculation, but when we are looking for the effects of the magnetic field, they should not be kept constant with changing value of the magnetic field since they are scaled in terms of the effective magnetic length.

Fig. 3.8 shows the net current for various magnetic fields, focusing particularly on the three different B-values $B = 0.0$ T (dotted black), $B = 0.5$ T (dashed blue) and $B = 1.0$ T (solid red). When the magnetic field increases the net current is seem to decrease is observed. The net current for $B = 1.0$ T still has an oscillation at the earlier time, then soon it goes to the steady state value, while for the other two cases the net current reaches to the steady state at a later time.

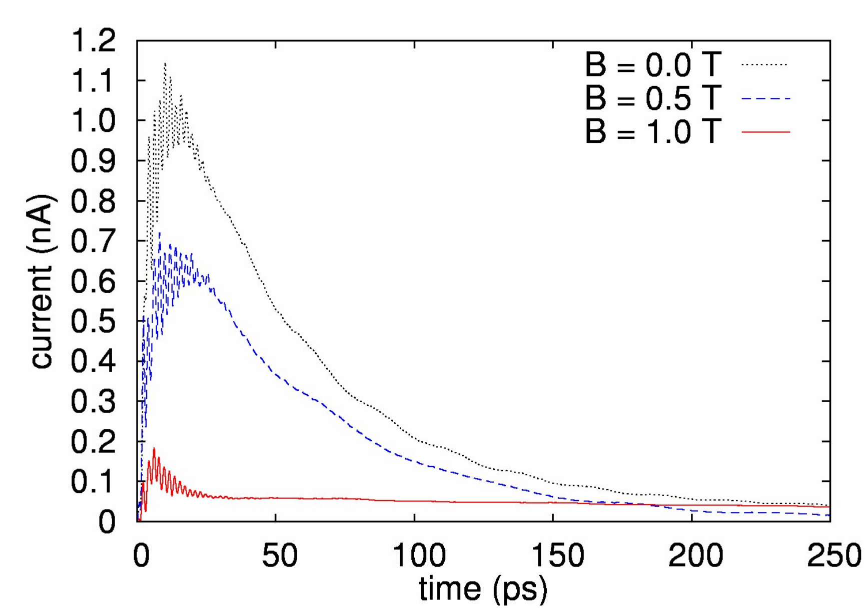

Figure 3.8: The noninteracting net current versus time for various magnetic field, for a double quantum wire with a coupling element

According to the behavior of the net current, we divided the net current oscillation into two time regimes, which are short-time τ_s regime and long-time τ_l regime. In the short time regime the net current has a strong oscillation with a short time period, while in the long time regime the oscillation becomes weaker and the time period is longer.

In the short time regime Fig. 3.9(a), an oscillation behavior is observed because electrons enter the sample from different subbands in the leads into more than one state in the central system. Another point about the oscillation behavior is that the oscillation could be relevant to the weak coupling contacts (there are not oscillations in the case of a strong coupling) [35].

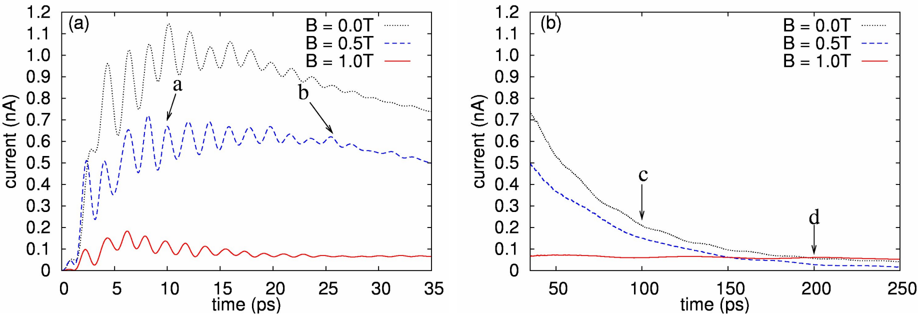

Figure 3.9: The noninteracting net current versus time for various magnetic field, for a double quantum wire with a coupling element

The time period in this regime is not affected by the magnetic field. However, the peak-to-peak amplitudes are influenced by the magnetic field, as the magnetic field changes the character of the energy spectrum (subbands) in the leads and the SESs in the sample are changed, as demonstrated in Fig. 3.7. We should mention that the two lower states in the sample are almost localized states (not shown) and at $B = 1.0$ T these are the only states in the bias window. In addition, the magnetic field increases the back scattering through the coupling element, however we know that in a simple geometry a magnetic field generally reduces backscattering.

In the long time regime Fig. 3.9(b), the oscillations of the net current are much slower and the time period become larger. For lower magnetic field $B = 0.0$ and 0.5 T the net current exponentially decreases up to ($t < 180$ ps) while for $B = 1.0$ T the net current is almost constant. After ($t > 180$ ps) the net current goes to the steady state for all three values of the magnetic field.

One more relevant physical parameter is the mean charge of the central system as shown in the Fig. 3.10. The total charge of the system is monotonically increasing with time, but when $B = 0.5$ T it seems to be faster approaching to a steady states, that is the reason why the net current for $B = 0.5$ T approaches steady states faster than $B = 1.0$ T. We note that the charging processes in the high magnetic field is slower than in a lower magnetic field.

To see the dynamics of electrons through the central DW system in the presence of different magnetic fields, we will show the many-electron charge distribution at $t = 10, 25.6, 100$, and 200 ps in Fig. 3.11, which are pointed by $\mathbf{a}-\mathbf{d}$ from Fig. 3.9. The charging process from the leads to the central system is observed from time ($t = t_0$). In the short time regime, at $t = 10$ ps the electrons are

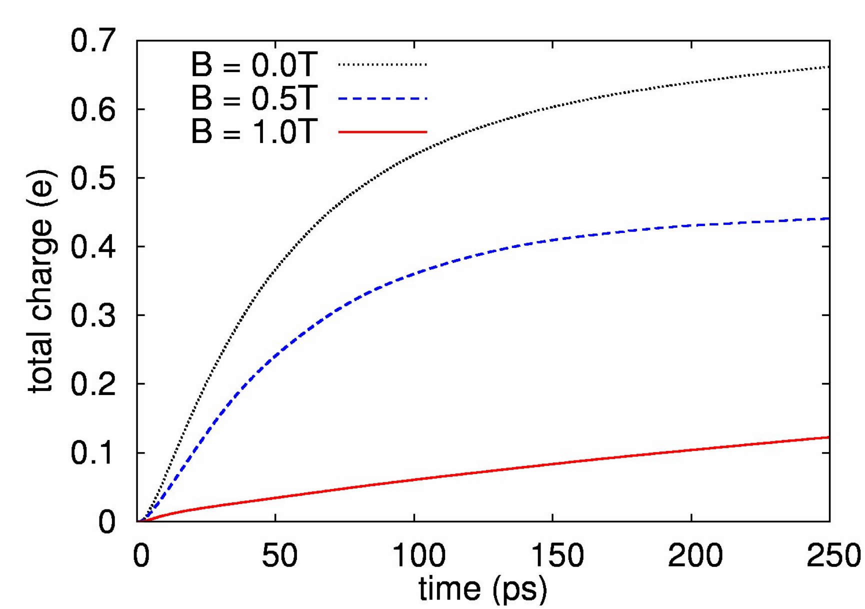

Figure 3.10: The total charge of the noninteracting system, for a double quantum wire with a coupling element

distributed through the DW system having oscillations and accumulating charge is observed in the window coupling element at $B = 0.0$ T, which easily happens because there is no Lorentz force pushing the electrons away from the center of the sample, but when we tune the magnetic field to $B = 0.5$ T the electron trajectories bend due to the Lorentz force, and the electrons go away from the coupling window. In that case electrons located in the right wire prefer to make interwire transfer as a backward or forward scattering to the left wire. When the magnetic field increases to $B = 1.0$ T the effective magnetic length becomes small compared to the length of the window, so the electrons totally transfer via interwire scattering as can be seen from the right to the left wire. At $t = 25.6$ ps the many-electron charge distribution continues with its oscillations in the absence of the magnetic field, while for $B = 0.5$ T the left to right wire backward-scattering occurs. At that time the many-electron charge density starts to make a ‘circular’ motion for $B = 1.0$ T.

In the long time regime, at time $t = 100$ ps the many-electron charge density spreads over the sample at $B = 0.0$ T, the same situation can be seen for higher magnetic field $B = 0.5$ T except at the window-coupling element, while the ‘circular’ cyclotron motion is present for $B = 1.0$ T. The many-electron charge distribution goes to the steady states without oscillation at $t = 200$ nm for all three cases.

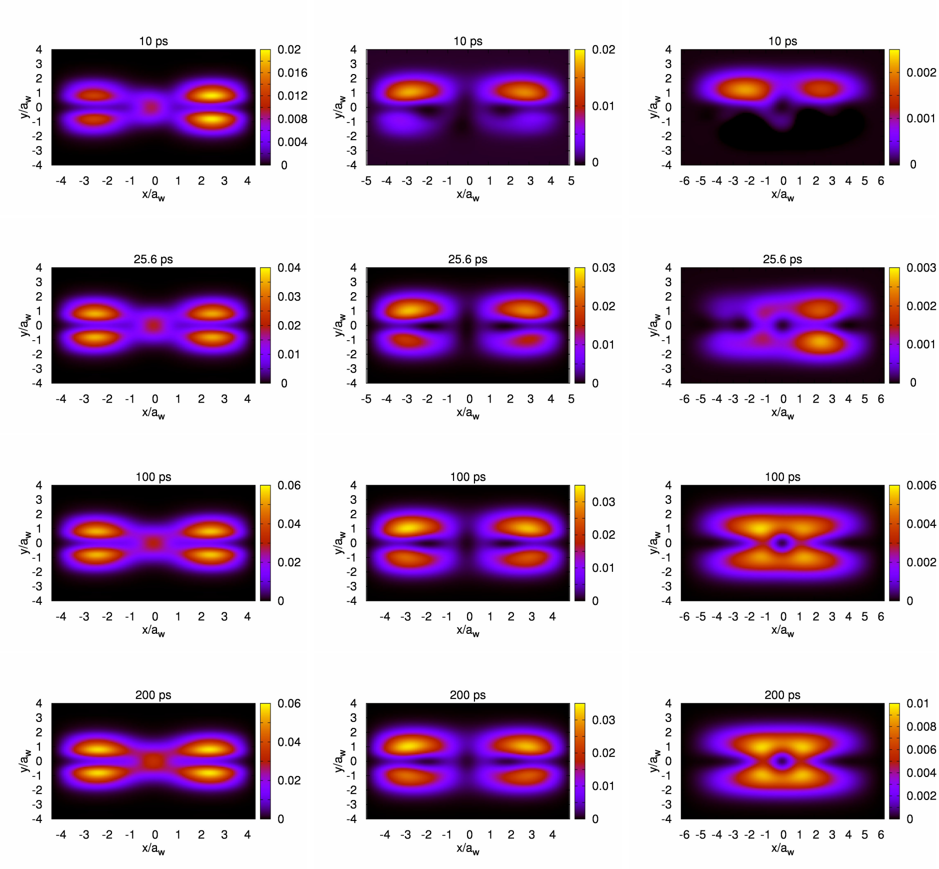

Figure 3.11: (Color online) The many-electron charge density for the noninteracting system. $B = 0.0$ T (left), $B = 0.5$ T (middle) and $B = 1.0$ T (right). The system is a double wire with a coupling element

3.2.2 Enhancement by the Coulomb interaction

We now describe the effects of the electron-electron interaction in the system. The Coulomb interaction in the system is important and in the case of a weak coupling it can lead to the so called Coulomb blockade, but there are finer details we want to investigate (e.g. quasi-localized charge in the coupling window). First we establish the left current I_L which describes the total current flowing from the left lead into the central sample through the left contact, and the right current I_R which displays the total current from the central sample into the right lead through the right contact.

In Fig. 3.12 the noninteracting left $I_{L,0}$ and right $I_{R,0}$ current, and the interacting left $I_{L,I}$ and right $I_{R,I}$ current are shown. We have recorded that the noninteracting and interacting left current are almost the same up to $t = 20$ ps, while for the noninteracting and interacting right current up to $t = 75$ ps are almost the same. Note that there is a small fluctuation in the right current in the earlier time which can occur because the sample is empty before the switching-on of the coupling between the sample and the leads, i.e. the electrons transferring from the right lead to the sample is observed.

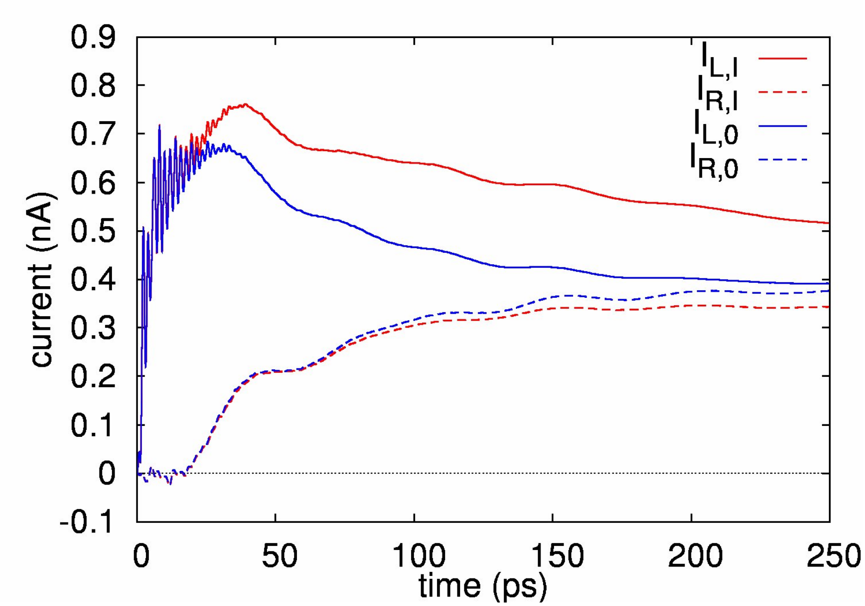

Figure 3.12: The noninteracting and the interacting left and right current for $B = 0.5$ T.

For better understanding the current oscillations, we separate the net current into two regimes.

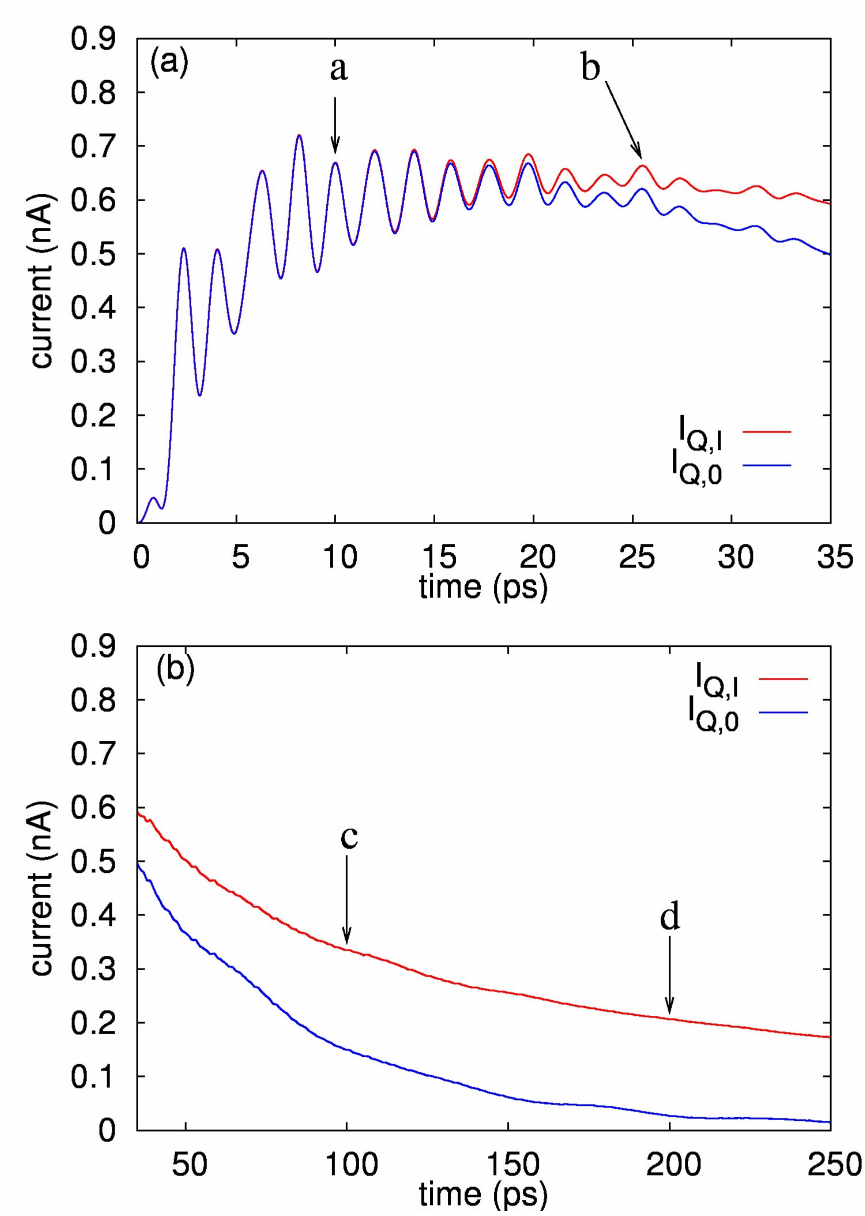

Figure 3.13: The noninteracting and the interacting net current for $B = 0.5$ T.

In Fig. 3.13(a), the short time regime, we provide both the non-interacting and the interacting net current as a function of time, where the net current $I_Q = I_L - I_R$. The peak-to-peak amplitude and the time period for the noninteracting net current $I_{Q,0}$ and the interacting net current $I_{Q,I}$ are the same with a rapid oscillation. The rapid oscillation with short period exhibits quantum interference. In this regime, the noninteracting and interacting currents are almost the same, the Coulomb correlation is unimportant as only a fraction of electron has entered the sample. For $t > 20$ ps the interacting net current is higher that the noninteracting case, as we see at $t = 35$ ps their distinction becomes ~ 0.1 nA.

In long time regime Fig. 3.13(b), the noninteracting $I_{Q,0}$ and interacting $I_{Q,I}$ net current are exponentially decreasing with time and a slow oscillation with long time period can be seen in this limit. The slow oscillation indicates the suppressing of the quantum interference feature. The Coulomb interaction enhances the current, the difference between noninteracting and interacting net current becomes 0.15 nA at $t = 200$ ps i.e. (the Coulomb correlation is 15%).

At a later time $t > 200$ ps, the noninteracting net current is approaching to the steady state while the interacting net current still doesn't go to the steady state, i.e. the time constants are longer for charging operation in the interacting case.

In Fig. 3.14 we plot the total charge for the noninteracting and interacting system. In both cases the total charge is monotonically increasing with time.

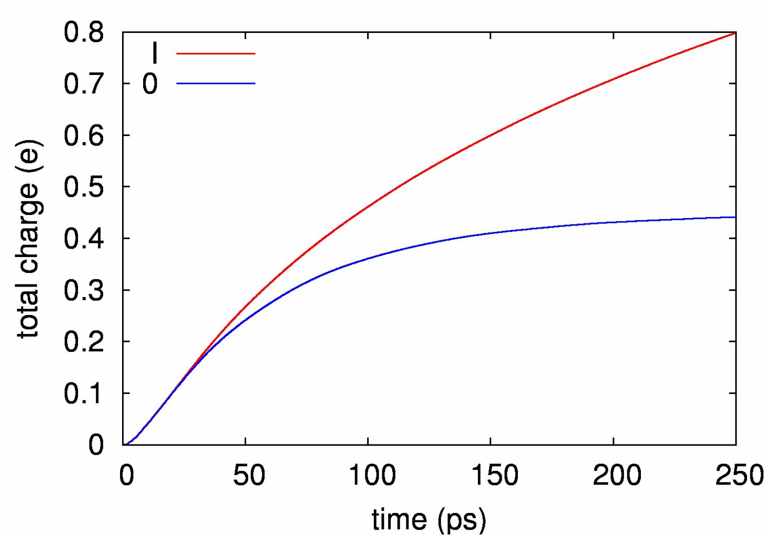

Figure 3.14: The total charge of the noninteracting (0) and interacting system (I). $B = 0.5$ T.

The blue line (blue solid) indicates the noninteracting total charge which seems to have reached the steady state after $t = 200$ ps, while for the interacting system (green solid) line the total charge still continues to increase. Note that the total charge for the interacting system is higher than the noninteracting system, at time $t = 250$ ps the interacting one is approximately twice higher than the noninteracting (the Coulomb correlation 36%). This indicates that the Coulomb interaction makes easier to draw electrons into central system.

In Fig. 3.15 we show the many-electron charge distribution for the noninteracting and the interacting system at the short time regime $t = 10, 25.6$ ps, and the long time regime $t = 100, 200$ ps, which are pointed out by $\mathbf{a} - \mathbf{d}$ in the Fig. 3.13. At time $t = 10$ and 25.6 ps electrons have a high probability to be backscattered from the right to the left wire, and the interwire scattering from the left to the right wire respectively. In this regime a slight charge accumulation is observed in the window-coupling elements for the interacting system at 25.6 ps.

At time $t = 100$ and 200 ps the many-electron charge distribution further goes to the steady states having a very small oscillation. We see that the Coulomb interaction makes a quasi-bound electron accumulation in the coupled-window with high density, while for the noninteracting case there is a circular empty region in the coupled element.

The two lowest SESs in the bias window are poorly coupled to the leads since they are localized in the coupling element in the middle of the system. The Coulomb interaction delocalizes these states and thus enhances the current through the system [36].

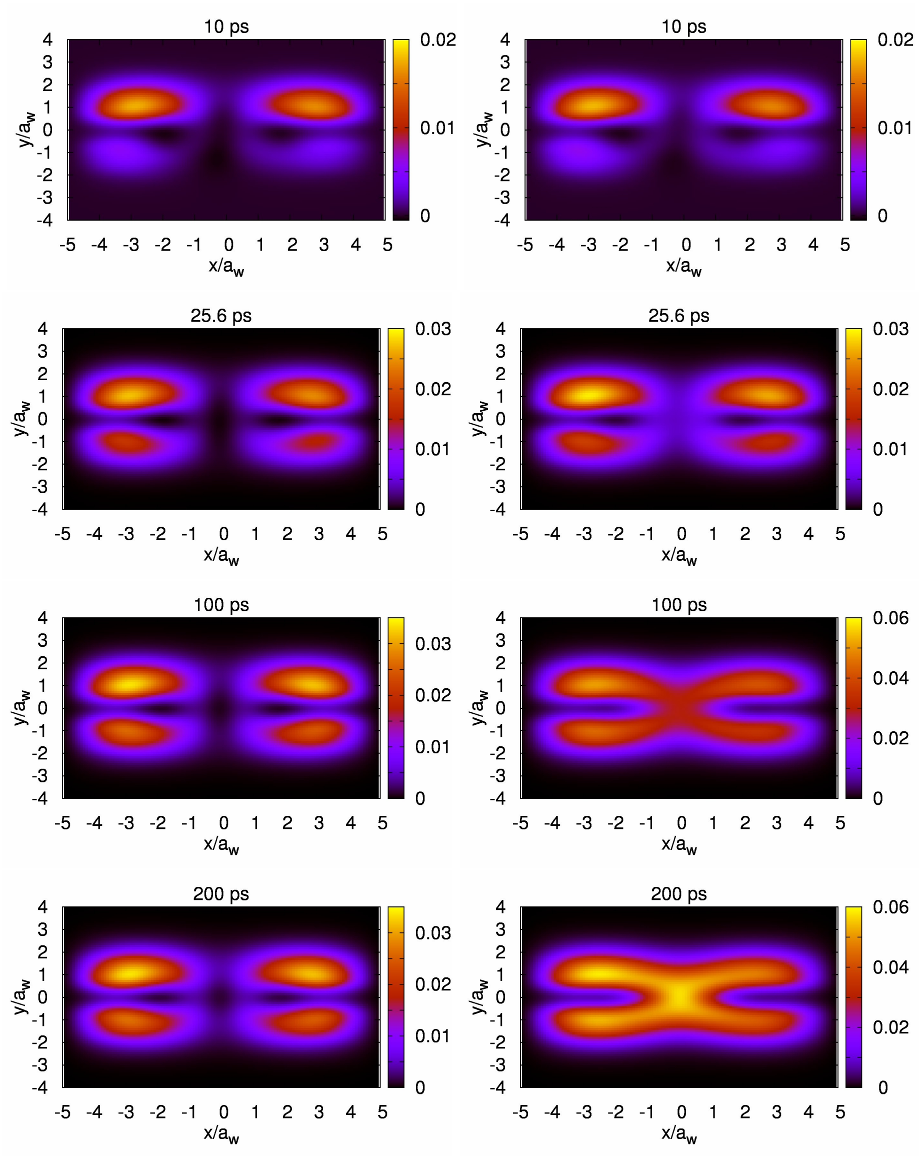

Figure 3.15: (Color online) The many-electron charge density for the noninteracting (left panel) and the interacting system (right panel). $B = 0.5$ T, $L_{\rm x} = 300$ nm, $L_{\rm w} = 100$ nm.

3.2.3 The size influence of the coupling element

The size of the coupling element between the wires does influence the transport properties of the system. A coupling window in the central system causes interwire backward scattering that suppressed the net current in the system. Fig. 3.16 displays the non-interacting net current for different sizes of the window. We have chosen three different lengths of the coupled-window $L_w = 0$ nm (dotted black), $L_w = 50$ nm (dashed blue), and $L_w = 100$ nm (solid red). We see that the net current for the system without a coupling window is higher than the net current with a window, since the interwire backscattering in the coupling window suppressed the net current.

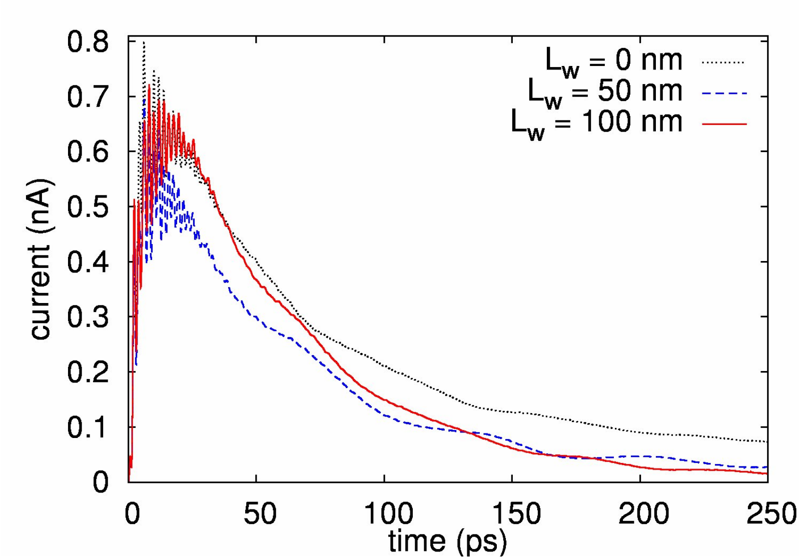

Figure 3.16: The non-interacting net current versus time for different size of the window , $B = 0.5$ T.

Now we turn on the Coulomb interaction in the central system, and observe what happens. In the short time regime Fig. 3.17(a) indicates that the interacting net current has strong oscillations. The net current is increasing and is almost the same up to $t = 2$ ps for all three cases. Later on, the net current starts it's oscillation behavior. We observed that the interacting net current in the presence of the coupling window of length $L_w = 100$ nm is higher than the net current without the window-coupling $L_w = 0$ nm, however the interwire backscattering is higher in the longer window, while the complete opposite situation happens in the absence of the Coulomb interaction. The reason is that the Coulomb interaction in the long window is more active in delocalizating the states in the window. We note that the net current for the shorter window $L_w = 50$ nm is smaller than the net current for $L_w = 100$ nm, and $L_w = 0$ nm. Here it is clear that the peak-to-peak amplitude and the period time do not change with varying the size of the window.

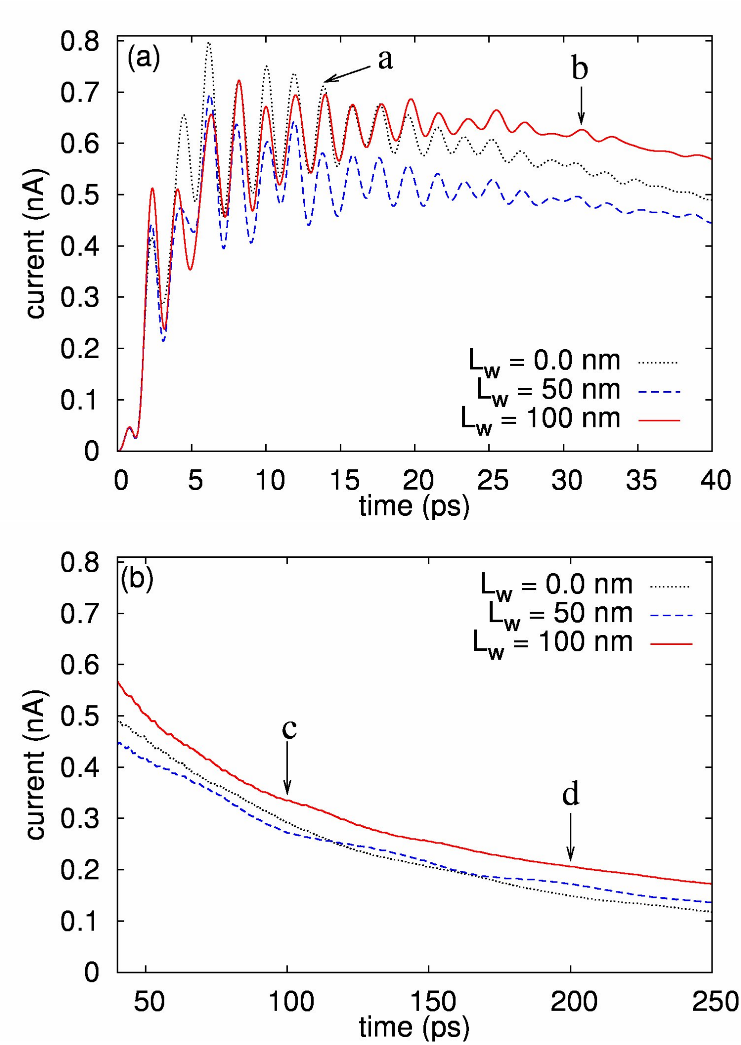

Figure 3.17: The interacting net current is plotted as a function of time for different size of the window, $B = 0.5$ T.

The net current in the long time regime, Fig. 3.17(b), exponentially decreases with time, having a very small oscillation and a long time period. The net current for $L_w = 100$ nm is high while the net current for $L_w = 50$ nm and $L_w = 0$ nm is lower. This implies that the Coulomb interaction has a great role in the transient dynamics for the long window. Another reason here is that the longer coupling-window lowers some of the states in the bias window and the Coulomb interaction makes them more accessible for transport.

To explain the charging processes for the three different window-sizes in the interacting system we display Fig. 3.18. The total charge for $L_w = 100$ nm is higher than the total charge for $L_w = 50$ nm and $L_w = 0$ nm. This implies that the charging for the longer window is faster.

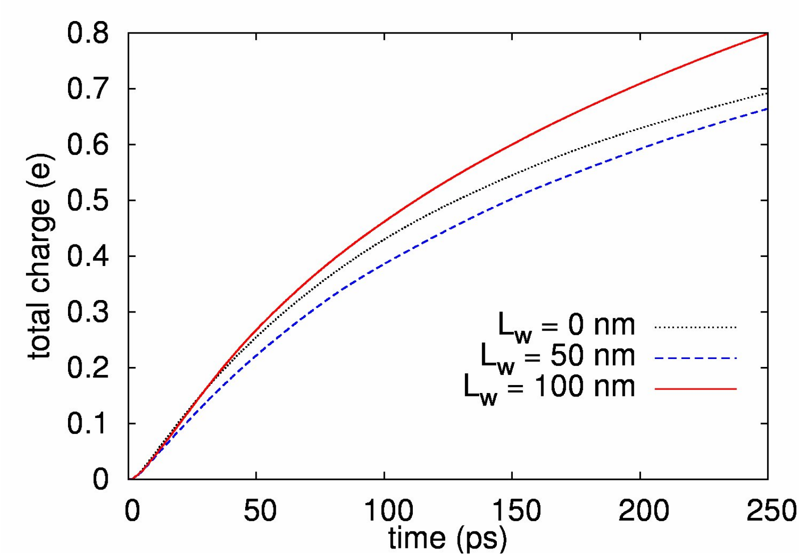

Figure 3.18: The interacting total charge versus time for different size of the window, $B = 0.5$ T.

In Fig. 3.19 the many-electron charge distribution for different sizes of the window is presented. The times $t = 14$ and 31.2 ps are pointed out by $\mathbf{a} - \mathbf{b}$ in the short time regime Fig. 3.17(a). The many-electron charge distributions has oscillation in the system, and the interwire backward scattering is presented in the window coupling. The accumulation of the many-electron charge density in the coupled-window $L_w = 100$ nm is higher than for $L_w = 50$ nm, because the Coulomb interaction more effectively couples the states of the window and states with more presence in the contact region. Furthermore without the window the charge distribution at $t = 14$ ps is almost only in the left wire which does occur due to the Lorentz force. At time $t = 100$ and 200 ps labeled by $\mathbf{c} - \mathbf{d}$ in the long time regime Fig. 3.17(b), the many-electron charge distribution continues to spread through the system with small oscillations. The charge in the coupling element is very high for $L_w = 100$ nm due to the delocalization of the Coulomb interaction, while for $L_w = 50$ nm it is lower.

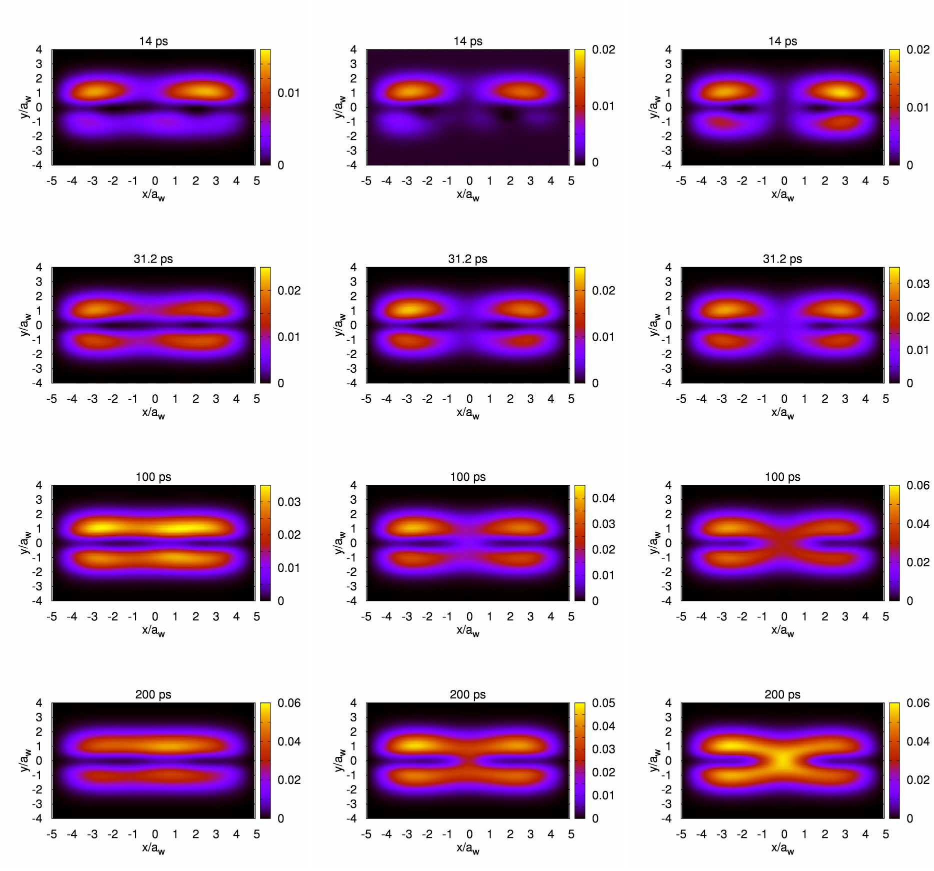

Figure 3.19: (Color online) The interacting many-electron charge distribution with different size of the coupling window: $L_\mathrm{w} = 0.0$ nm (left), $L_\mathrm{w} = 50$ nm (middle), and $L_\mathrm{w} = 100$ nm (right). $B = 0.5$ T.

3.2.4 The nonlocal coupling geometry

Now we briefly discuss the effect of the nonlocal coupling strength Γ^l on the net current dynamics. We keep the nonlocal coupling strength $\Gamma^l = 4g_0^l a_w^{3/2}/(\delta_x^l \delta_y^l)^{1/2} = 54.5$ meV.nm^2, a constant value. We take three different profile bandwidths of the coupling function by changing the parameters of the nonlocal coupling strength. The parameters are presented in Table 3.1, where the unit of δ_x and δ_y is nm^{-2}.

Table 3.1: The parameters of the nonlocal coupling strength

coupling function	coupling strength $\left(\frac{2g_0^l a_w^{3/2}}{\sqrt{\delta_y^l}}\right)$	nonlocal effect $\left(\frac{2}{\sqrt{\delta_x^l}}\right)$
Γ_1	$g_0^l a_w^{3/2} = 60,\ \ \delta_y^l = 4.4\times10^{-4}$	$\delta_x^l = 4.4\times10^{-4}$
Γ_2	$g_0^l a_w^{3/2} = 30,\ \ \delta_y^l = 1.1\times10^{-4}$	$\delta_x^l = 4.4\times10^{-4}$
Γ_3	$g_0^l a_w^{3/2} = 15,\ \ \delta_y^l = 0.275\times10^{-4}$	$\delta_x^l = 4.4\times10^{-4}$

With these parameters, the profile of the coupling function in the y-direction is potted and shown in Fig 3.20, while we keep the nonlocal effect in x-direction fixed.

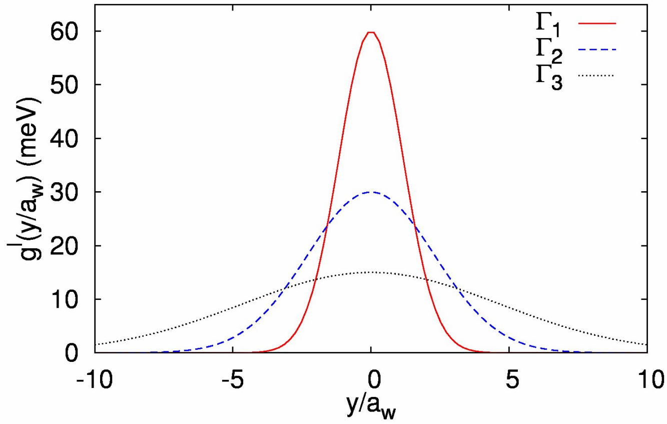

Figure 3.20: The profile of the coupling strength in the y-direction. $B = 0.5$ T.

The transient current rises suddenly after switching on the contacts. We observed that decreasing the bandwidth of the coupling function, the current becomes higher as displayed in Fig 3.21.

In the short time regime Fig 3.21(a), the peak-to-peak amplitude of the oscillation decreases as the bandwidth of the coupling function increases, while the period time is independent of the change. A broad coupling function in the y-direction favors coupling to higher subbands and edge states, but lowers the coupling to the band edge of the first subband in the leads.

In long time regime Fig 3.21(b), the steady state is reached faster with increasing bandwidth of the coupling.

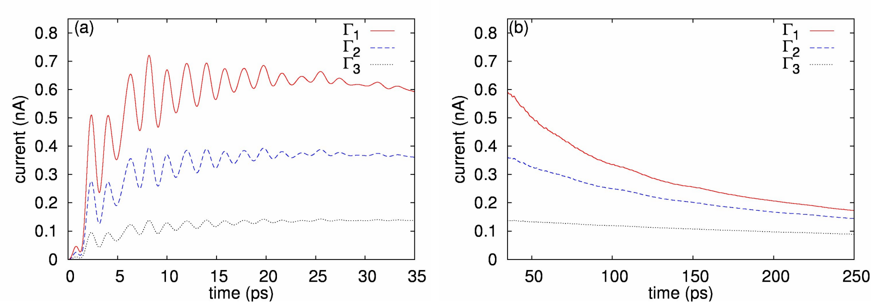

Figure 3.21: The interacting net current versus time for various nonlocal coupling strength. $B = 0.5$ T, $L_x = 300$ nm, $L_w = 100$ nm.

The interacting many-electron charge distributions compared in Fig 3.22 at $t = 200$ ps confirm that the best coupling is to have a narrower coupling function, because in that case the charging processes and the interwire transfer is much higher than for the broader coupling. The charge accumulation and quasi-localized charges in the window element is very high for a narrower coupling function in the interacting system.

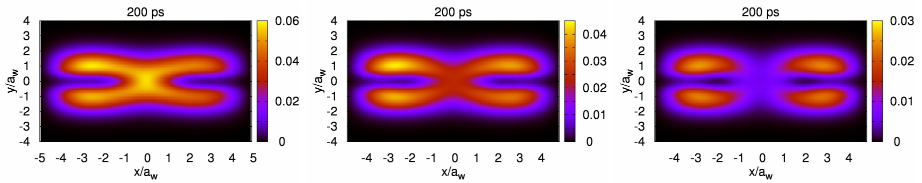

Figure 3.22: (Color online) The interacting many-electron charge distribution. Γ_1 (left), Γ_2 (middle) and Γ_3 (right). $B = 0.5$ T, $L_x = 300$ nm, $L_w = 100$ nm.

3.3 Double wire with a double coupling-window elements

The last nanostructure that we investigate is a parallel laterally double quantum wire of length L_x with a double window-elements (DWW) in the barrier between them. The potential defining the DWW subsystem with the coupling elements is described by

$$V_{\rm DW}(\mathbf{r}) = V_{\rm MB}(y) + V_{\rm CW}(x,y), \tag{3.6}$$

where

$$V_{\rm MB}(y) = V_B\, e^{(-\beta^2(y-y_0)^2)}, \tag{3.7}$$

and

$$V_{\rm CW}(x,y) = -\sum_{i=1}^{2} V_{W_i}\, e^{(-\beta_{x_i}^2(x-x_i)^2-\beta_{y_i}^2(y-y_i)^2)}. \tag{3.8}$$

Fig. 3.23 indicates the double nanowires with a double window-coupling system. The parameters are,

- $V_B = 16$ meV, $\beta = 0.15$ nm^{-1}, $y_0 = 0\, a_w$
- $V_{W_1} = 16$ meV, $\beta_{x_1} = 0.04$ nm^{-1}, $\beta_{y_1} = 0.15$ nm^{-1}, $x_1 = 2.0\, a_w$, $y_1 = 0\, a_w$.
- $V_{W_2} = 16$ meV, $\beta_{x_2} = 0.04$ nm^{-1}, $\beta_{y_2} = 0.15$ nm^{-1}, $x_2 = 2.0\, a_w$, $y_2 = 0\, a_w$.

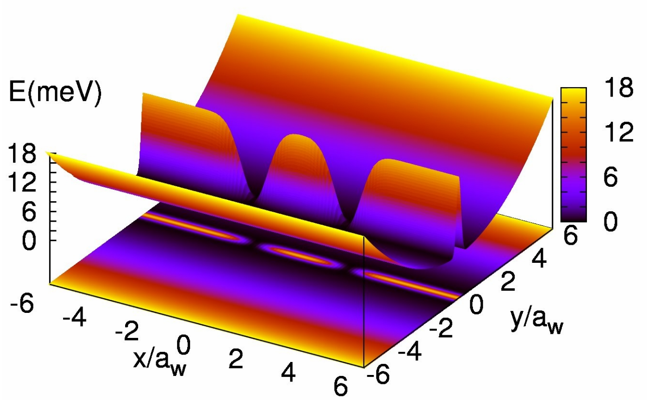

Figure 3.23: (Color online) Schematic representation of the potentail defining the parallel double wire with a double window-coupling system. $B = 0$ T, $L_{\rm x} = 300$ nm, $L_{\rm w} = 50$ nm, and $\hbar\Omega_0 = 1.0$ meV.

We assume that the chemical potentials $\mu_L = 2.3$ meV and $\mu_R = 1.6$ meV are fixed. This provides a constant bias window $\mu_L - \mu_R = -eV_{\text{bias}} = 0.7$ meV. The extention parameter ($\Delta = 0.3$ meV) which is the extended bias window to give the window of relevant states $\Delta\mu + 2\Delta = 1.3$ meV.

Contributing to the transport are *eight* SESs distributed as follows: the six lowest states are located in the active bias window $[\mu_L, \mu_R]$, while the other two states are located in the top of the extended bias window $[\mu_L, \mu_L + \Delta]$. One subband in the leads is located in the relevant bias window (not shown).

We now compare the noninteracting ($I_{Q,0}$) and interacting ($I_{Q,I}$) time-dependent net currents for the DWW system in Fig. 3.24. Besides the net current we plot the noninteracting left current $I_{L,0}$ which describes the total current flowing from the left lead into the central system, and the noninteracting right current $I_{R,0}$ indicating the total current flowing from the central system into the right lead.

After switching-on the coupling at $t = t_0$, the leads start the charging process into the sample up to $t = 10$ ps . Later on, the left and the right current are approaching the steady states having small oscillations in the right current.

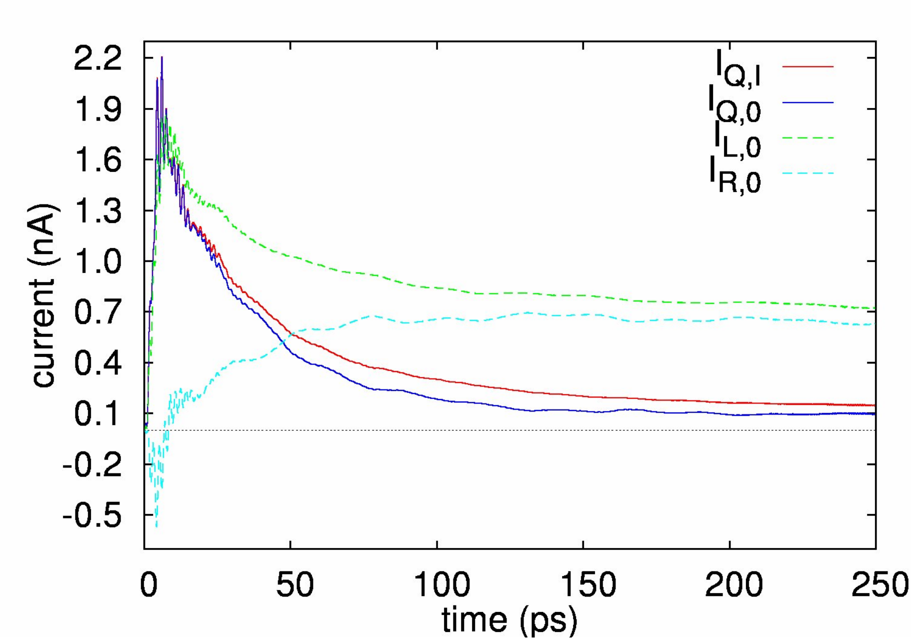

Figure 3.24: The noninteracting and interacting net current versus time for $B = 1.0$ T.

The noninteracting and interacting net current is increasing up to $t = 20$ ps exhibiting oscillations, but not as strong as in the system with a single coupling-element, then the net current exponentially decreases with time up to $t = 150$ ps. The difference between noninteracting and interacting currents becomes 0.07 nA (The Coulomb correlation $\sim 7\%$) at $t = 250$ ps when the system is approaching the steady state.

Fig. 3.25 shows the noninteracting and interacting total charge, a similar enhancement in the total charge is observed as in the interacting DWW system, the Coulomb correlation is 18% at $t = 250$ ps. It means that the Coulomb interaction facilitates the entrance of the electrons into the central system. The same effect, as we have observed in the system with low lying localized states away from the contact region.

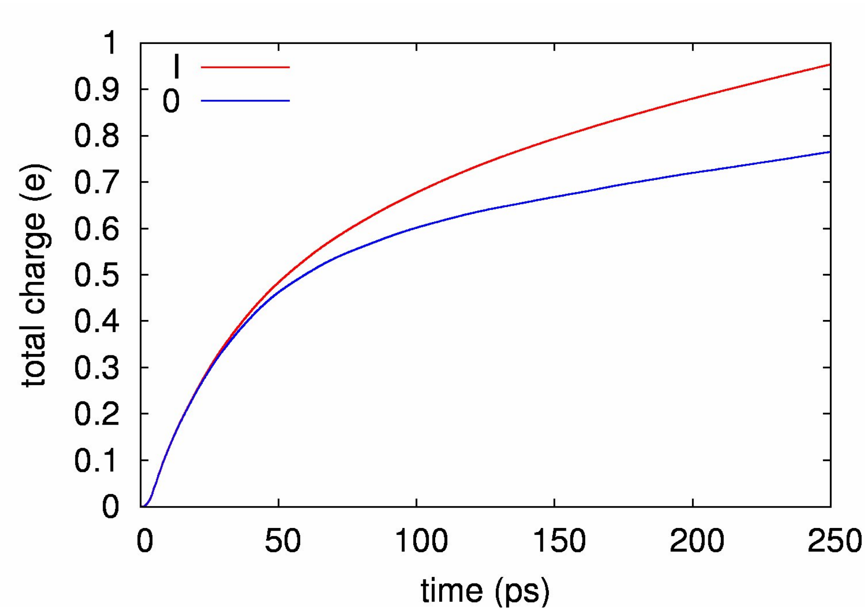

Figure 3.25: The total charge of the noninteracting (0) and interacting system (I). $B = 1.0$ T.

The many-electron charge distributions in the central system compared in Fig. 3.26 displays the noninteracting (left panel) and interacting (right panel) system at $t = 4, 20, 100$ and 220 ps. At early time $t = 4$ ps, the wires seem to be able to exchange charge between the left and the right wire through both the coupling elements independently. We should note that there is no backscattering process to the contacts in the many-electron charge motion here, because just after switching-on the coupling a quasi-localized many-electron charge distribution appears in the windows for both noninteracting and interacting system. At $t = 20$ ps the many-electron charge is moving from the left window to the right window, mostly through the left wire, which gives us a nice oscillation between both windows as a ‘dipole’ oscillation. The Coulomb interaction slightly affect the charge density in the windows.

Later on, at time $t = 100$ and 220 ps the many-electron charge is localized in the windows. Note that a ’circular’ motion can not be seen here because the length of the central barrier is 120 nm which is larger that the magnetic length at $B = 1.0$ T, but the charge distribution suggests a cyclotron motion of a more complex structure.

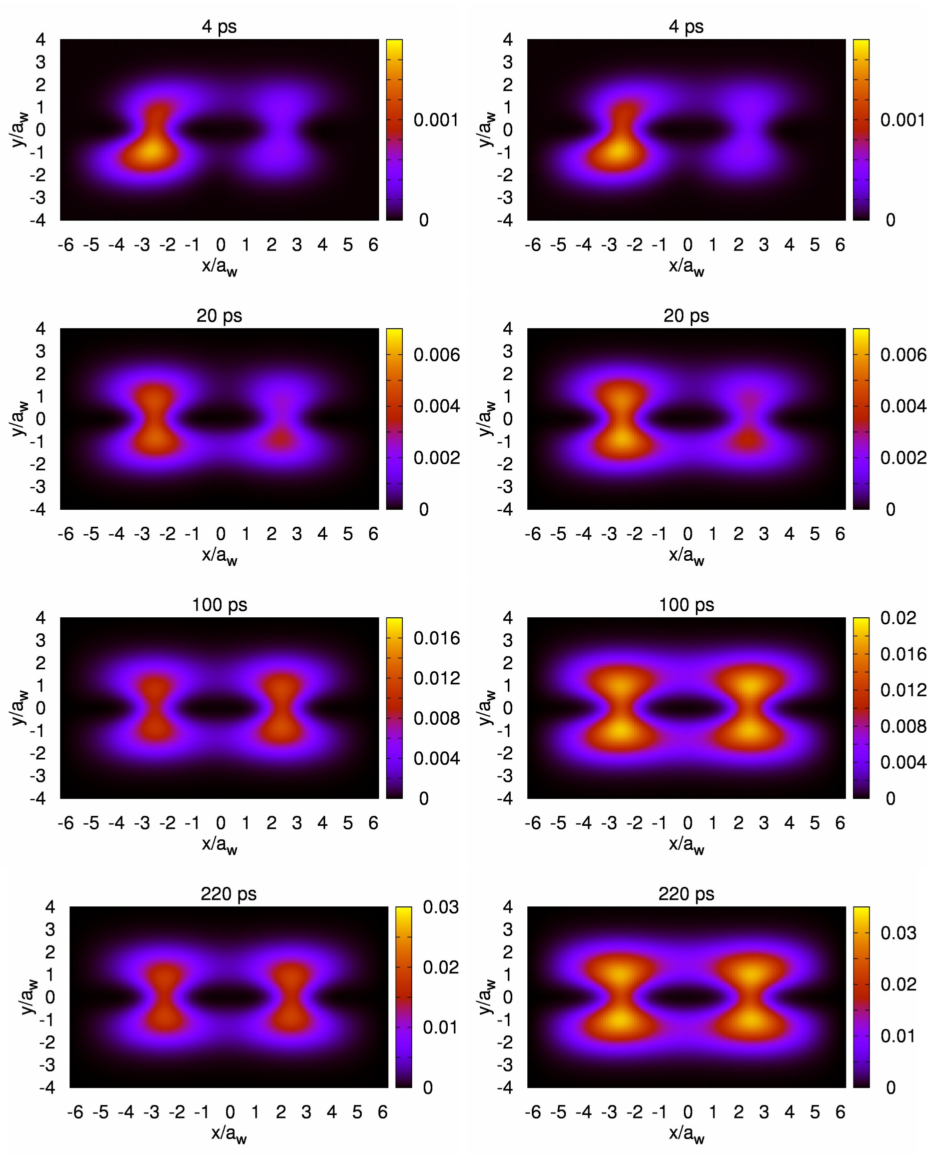

Figure 3.26: (Color online) The many-electron charge density for the noninteracting (left panel) and the interacting system (right panel). $B = 1.0$ T, $L_x = 300$ nm, and $L_w = 50$ nm.

Chapter 4

Summary and Conclusion

To summarize, we have presented a quantum general master equation formalism to investigate time-dependent transport through open mesoscopic systems composed of a finite sample connected to two semi-infinite leads via contact regions in an external magnetic field. The electron-electron interaction was included in the central sample, but neglected in the leads. The Coulomb interaction was treated in a many-body description using an exact diagonalization method, in a truncated many-body Fock-space using the state basis of the non-interacting system.

We used three different geometries of the central system, a parallel double wire, a parallel double wire with a single coupling window, and a parallel double wire with a double coupling window. In the first structure, we demonstrated that the net current and the many-electron charge distribution were enhanced by the Coulomb interaction with a rate of (10%) in the long time regime.

The second structure was a richer structure due to the observation of the interference phenomenon between the wires through the window-coupling. We have demonstrated that the Coulomb interaction doesn't have a great role in the short time regime while the inter-wire backward scattering feature was dominant. In addition, the net current is enhanced in the interacting system (Coulomb correlation 15%), which was higher than the Coulomb correlation (10%) of the lateral double wire system. A quasi-localized many-electron charge distribution was induced in the coupled-window interacting system.

In the third structure, however we had a higher bias window but the net current in the interacting system is not enhanced very much due to localization of the electron charge in the windows coupled for both noninteracting and interacting system. Moreover, the inter-wire backward scattering into the contacts is not active in this system.

The magnetic field had a great effect on the net current in the double wire with a coupling window system. As the magnetic field increased the inter-wire backward scattering into the contacts was increased through the coupling windows, and the net current was suppressed in the system, while we know that generally a magnetic field decreases backscattering. In addition with increasing magnetic field the energy spectrum shifted up, and fewer single electron states participated in the transport, so the net current was suppressed.

The conceived mesoscale coupling window system could serve as an elementary quantum device for sensitive spectroscopy tools for electrons and quantum information processing by controlling the coupling window and the applied magnetic field.

Appendix A

Single electron

In this appendix an analytical derivation of the single electron model will be shown.

A.1 Central system

For an isolated sample ($t < t_0$), the single-electron Hamiltonian is

$$h_{\mathrm{Sample}} = h_{\mathrm{S}} + V_{\mathrm{DW}}(\mathbf{r}). \tag{A.1}$$

We will describe the Hamiltonian of the pure and the embedded quantum wire.

A.1.1 Single finite wire

First we calculate the eigenvalues and wavefunctions of the non-perturbed wire. Non-perturbed Hamiltonian of a quantum wire in an external perpendicular magnetic field can be described by

$$h_{\mathrm{S}} = \pi^2/2m^* + V_{\mathrm{h}}(x) + V_{\mathrm{p}}(y), \tag{A.2}$$

where $\pi = p + e\mathbf{A}$ is the kinetic term, and the confining potentials $V_{\mathrm{h}}(x)$ and $V_{\mathrm{p}}(y)$ denote the hard wall and the parabolically confinement potential respectively, which are given by

$$V_{\mathrm{h}}(x) = \begin{cases} 0, & \text{if } |x| < \dfrac{L_x}{2}, \\ \\ \infty, & \text{if } |x| \geq \dfrac{L_x}{2}, \end{cases} \tag{A.3}$$

and

$$V_{\mathrm{p}}(y) = \frac{1}{2} m^* \Omega_0^2 y^2. \tag{A.4}$$

The central system is finite with x in the interval $[-L_x/2, L_x/2]$. One can write the Hamiltonian of the non-perturbed single-electron central system as

$$h_{\mathrm{S}} = \frac{1}{2m^*} \left[p + e\mathbf{A} \right]^2 + \frac{1}{2} m^* \Omega_0^2 y^2, \tag{A.5}$$

if we choose a homogenous magnetic field $\vec{B}$ to be in the z-direction ($\vec{B} = Bz$), described in the Landau gauge by a vector potential $\mathbf{A} = (-By, 0, 0)$. The Hamiltonian is expressed as

$$h_{\mathrm{S}} = \frac{1}{2m^*} \left[\frac{\hbar}{i} \nabla - eBy\vec{x} \right]^2 + \frac{1}{2} m^* \Omega_0^2 y^2, \tag{A.6}$$

expanding the square bracket in the first term one has

$$h_{\mathrm{S}} = -\frac{\hbar^2}{2m^*} \left(\Delta^2 - \frac{2i}{\ell^2} y \partial_x - \frac{y^2}{\ell^2} \right) + \frac{1}{2} m^* \Omega_0^2 y^2 \tag{A.7}$$

where $\ell^2 = \hbar/eB = \hbar/m^* \omega_c$ is the magnetic length. The Hamiltonian can be reorganized as

$$h_{\mathrm{S}} = \frac{p_{\mathrm{x}}^2}{2m^*} + \frac{p_{\mathrm{y}}^2}{2m^*} + \frac{1}{2} m^* \Omega_w^2 y^2 + \omega_c y p_x. \tag{A.8}$$

$\Omega_w^2 = \Omega_0^2 + \omega_c^2$ and $p_x = (\hbar/i)\partial_x$. Eq. (A.8) is the time-independent Hamiltonian of the central system, so a two-dimensional Schrödinger equation is

$$h_{\mathrm{S}} \psi_n^{\mathrm{S}}(x,y) = E_n \psi_n^{\mathrm{S}}(x,y), \tag{A.9}$$

where $\psi_n^{\mathrm{S}}(x,y)$ and E_n are the single electron wave functions and the eigenvalues of the central sample respectively. Using boundary conditions (a) $\psi_n^{\mathrm{S}}(-\frac{L_x}{2}, y) = \psi_n^{\mathrm{S}}(\frac{L_x}{2}, y) = 0$ and (b) $\psi_n^{\mathrm{S}}(x, y \to \pm\infty) = 0$, with Eq. (A.9) suggests that the wave functions can be expanded as

$$\Psi_n^{\mathrm{S}} = \sum_{n_x, n_y} C_{n_x}^{n_y} \varphi_{n_x}(x) \phi_{n_y}(y), \tag{A.10}$$

where $\varphi_{n_x}(x)$ and $\phi_{n_y}(y)$ are the complete basis wave functions Eq (2.7) and Eq (2.8).

To calculate the matrix elements of the Hamiltonian of the central system we divide Eq. (A.8) into three parts

$$h_{\mathrm{S}} = h_{\mathrm{x}} + h_{\mathrm{y}} + h_{\mathrm{xy}}, \tag{A.11}$$

herein, $h_{\mathrm{x}} = p_{\mathrm{x}}^2/2m^*$, $h_{\mathrm{y}} = p_{\mathrm{y}}^2/2m^* + (1/2)m^*\Omega_w^2 y^2$ and $h_{\mathrm{xy}} = \omega_c y p_x$. Using the Dirac notation we will get the matrix elements

$$\langle \psi_n^{\mathrm{S}} | h_{\mathrm{S}} | \psi_n^{\mathrm{S}} \rangle = \langle \psi_n^{\mathrm{S}} | h_{\mathrm{x}} + h_{\mathrm{y}} + h_{\mathrm{xy}} | \psi_n^{\mathrm{S}} \rangle, \tag{A.12}$$

with the following results

$$\langle \psi_n^{\mathrm{S}} | h_{\mathrm{x}} | \psi_n^{\mathrm{S}} \rangle = \frac{n_x^2 \pi^2}{2} \left(\frac{a_w^2}{L_x} \right)^2 (\hbar\Omega_{\mathrm{w}}) \delta_{n_x,n_x^{'}} \delta_{n_y,n_y^{'}}, \tag{A.13}$$

$$\langle \psi_n^{\mathrm{S}} | h_{\mathrm{y}} | \psi_n^{\mathrm{S}} \rangle = \left(n_y^{'} + \frac{1}{2} \right) (\hbar\Omega_{\mathrm{w}}) \delta_{n_x,n_x^{'}} \delta_{n_y,n_y^{'}}, \tag{A.14}$$

and

$$\langle \psi_n^{\mathrm{S}} | h_{\mathrm{xy}} | \psi_n^{\mathrm{S}} \rangle = i\hbar\omega_{\mathrm{c}} a_w \, I_{n_x,n_x^{'}} \left[\sqrt{\frac{n_y^{'}}{2}} \delta_{n_y,n_y^{'}-1} + \sqrt{\frac{n_y^{'}+1}{2}} \delta_{n_y,n_y^{'}+1} \right], \tag{A.15}$$

where

$$I_{n_x,n_x^{'}} = \begin{cases} \dfrac{4 n_x n_x^{'}}{(n_x^2 - n_x^{'2}) L_x} \sin\left(\dfrac{n_x^{'}\pi}{2} \right) \cos\left(\dfrac{n_x \pi}{2} \right), & \text{if } n_x = \text{even},\ n_x^{'} = \text{odd} \\[2ex] \dfrac{4 n_x n_x^{'}}{(n_x^2 - n_x^{'2}) L_x} \sin\left(\dfrac{n_x \pi}{2} \right) \cos\left(\dfrac{n_x^{'}\pi}{2} \right), & \text{if } n_x = \text{odd},\ n_x^{'} = \text{even}. \end{cases}$$

combining these we obtain the matrix elements of the non-perturbed central wire in a magnetic field

$$\langle \psi_n^{\mathrm{S}} | h_{\mathrm{S}} | \psi_n^{\mathrm{S}} \rangle = \delta_{n_x n_x^{'}} \delta_{n_y n_y^{'}} \, \hbar\Omega_w \, \Xi^0_{n_x,n_y^{'}} + \hbar\omega_c \, i \, a_w I_{n_x,n_x^{'}} \, \Xi^{\mathrm{B}}_{n_y^{'},n_y}, \tag{A.16}$$

herein,

$$\Xi^0_{n_x,n_y^{'}} = \left[\frac{1}{2} \left(\frac{n_x \pi a_w}{L_x} \right)^2 + \left(n_y^{'} + \frac{1}{2} \right) \right],$$

and

$$\Xi^{\mathrm{B}}_{n'_y,n_y} = \left[\sqrt{\frac{n'_y}{2}}\,\delta_{n_y,n'_y-1} + \sqrt{\frac{n'_y+1}{2}}\,\delta_{n_y,n'_y+1} \right].$$

Eq. (A.16) are the matrix elements, which yield the discrete energy spectrum of the central sample.

A.1.2 Embedded finite wire

In this section, we briefly present the matrix elements of the embedded potential. We have shown that the embedded double quantum wire subsystem DW V_{DW} is described by

$$V_{\mathrm{DW}}(\mathbf{r}) = V_{\mathrm{MB}}(y) + V_{\mathrm{CW}}(x,y). \tag{A.17}$$

We will focus here on the calculation of the matrix elements

$$\langle n'|V_{\mathrm{DW}}|n\rangle = \langle n'|(V_{\mathrm{MB}} + V_{\mathrm{CW}})|n\rangle. \tag{A.18}$$

Matrix elements of the middle barrier potential

The potential barrier separating the double lateral wires has the following form

$$V_{\mathrm{MB}}(y) = V_B\, e^{(-\beta_0^2(y-y_0)^2)}, \tag{A.19}$$

the matrix elements of the barrier potential are

$$\langle n'|V_{\mathrm{MB}}|n\rangle = V_{\mathrm{MB}\ n';n} = \delta_{n'_x,n_x} V_{n'_y;n_y}, \tag{A.20}$$

where

$$V_{n'_y;n_y} \;= \int dy\ \phi^*_{n'_y}(y)\ V_{\mathrm{MB}}(y)\ \phi_{n_y}(y). \tag{A.21}$$

Using the basis wave functions $\phi_{n_y}(y)$ one can get

$$\begin{aligned} V_{n'_y;n_y} = &\left(\frac{V_{\mathrm{B}}}{a_w [2^{(n_y+n'_y)}\ n_y! n'_y!\ \pi]^{\frac{1}{2}}} \right) \int dy\, \mathrm{H}_{n'_y}(y/a_w) \mathrm{H}_{n_y}(y/a_w) \\ &\times e^{(-\beta_0^2 a_w^2((y/a_w)-(y_0/a_w))^2-(y/a_w)^2)}. \end{aligned} \tag{A.22}$$

We shall use $u = y/a_w$ and $\tilde{\beta}_0 = \beta_0^2 a_w^2$, to simplifying the matrix elements

$$V_{n'_y;n_y} = \frac{V_{\mathrm{B}}}{[2^{(n_y+n'_y)}\ n_y! n'_y!\ \pi]^{\frac{1}{2}}} \int du\, e^{-(\tilde{\beta}_0(u-u_0)^2+u^2)}\ \mathrm{H}_{n'_y}(u) \mathrm{H}_{n_y}(u). \tag{A.23}$$

To perform the integral we need

$$\begin{aligned}
\tilde{\beta}_0(u-u_0)^2+u^2 &= \tilde{\beta}_0 u^2 - 2\tilde{\beta}_0 u u_0 + \tilde{\beta}_0 u_0^2 + u^2 \\
&= \tilde{\beta}_0 u^2 - 2\tilde{\beta}_0 u u_0 + \tilde{\beta}_0 u_0^2 + u^2 - \frac{\tilde{\beta}_0 u_0^2}{1+\tilde{\beta}_0} + \frac{\tilde{\beta}_0 u_0^2}{1+\tilde{\beta}_0} \\
&= -\left[(1+\tilde{\beta}_0)^{\frac{1}{2}} u - \frac{\tilde{\beta}_0 u_0}{(1+\tilde{\beta}_0)^{\frac{1}{2}}}\right] - \frac{\tilde{\beta}_0 u_0^2}{1+\tilde{\beta}_0},
\end{aligned}$$

let's use $z = (1+\tilde{\beta}_0)^{\frac{1}{2}} u,$ and rearrange the terms, then Eq. (A.23) is transformed into

$$\begin{aligned}
V_{n'_y;n_y} = {} & \frac{V_{\mathrm{B}}}{[2^{(n_y+n'_y)}\, n_y! n'_y!\ \pi]^{\frac{1}{2}}} \frac{e^{-[\tilde{\beta}_0 u_0^2/(1+\tilde{\beta}_0)]}}{(1+\tilde{\beta}_0)^{\frac{1}{2}}} \\
& \times \int dz\, e^{-[z-\tilde{\beta}_0 u_0/(1+\tilde{\beta}_0)^{\frac{1}{2}}]^2}\, \mathrm{H}_{n'_y}\left(\frac{z}{(1+\tilde{\beta}_0)^{\frac{1}{2}}}\right) \mathrm{H}_{n_y}\left(\frac{z}{(1+\tilde{\beta}_0)^{\frac{1}{2}}}\right). \qquad \text{(A.24)}
\end{aligned}$$

Using the identity of the Hermite polynomials

$$\begin{aligned}
\int dz e^{-(z-z_0)^2} \mathrm{H}_{m'}(\alpha z) \mathrm{H}_m(\alpha z) = {} & \pi^{\frac{1}{2}} \sum_{k=0}^{min(m,m')} 2^k\, k! \binom{m}{k} \binom{m'}{k} \\
& \times (1-\alpha^2)^{(\frac{m+m'}{2}-k)}\, \mathrm{H}_{m+m'-2k}\left(\frac{\alpha z_0}{(1-\alpha^2)^{\frac{1}{2}}}\right).
\end{aligned} \qquad \text{(A.25)}$$

and comparing Eq. (A.24) with Eq. (A.25), we explicity get with $\alpha = 1/(1+\tilde{\beta}_0)^{\frac{1}{2}}$, that Eq. (A.24) is transformed to the following form

$$\begin{aligned}
V_{n'_y;n_y} = {} & \frac{V_{\mathrm{B}}}{[2^{(n_y+n'_y)}\, n_y! n'_y!]^{\frac{1}{2}}} \frac{e^{-[\tilde{\beta}_0 u_0^2/(1+\tilde{\beta}_0)]}}{(1+\tilde{\beta}_0)^{\frac{1}{2}}} \sum_{k=0}^{min(n_y,n'_y)} 2^k\, k! \binom{n_y}{k} \binom{n'_y}{k} \\
& \times \left(\frac{\tilde{\beta}_0}{(1+\tilde{\beta}_0)}\right)^{(\frac{n_y+n'_y}{2}-k)} \mathrm{H}_{n_y+n'_y-2k}\left(\frac{\tilde{\beta}_0^{\frac{1}{2}} u_0}{(1+\tilde{\beta}_0)^{\frac{1}{2}}}\right). \qquad \text{(A.26)}
\end{aligned}$$

Finally using the values $u = y/a_w$ and $\tilde{\beta}_0 = \beta_0^2 a_w^2$ to get the matrix elements of the barrier potential

$$V_{n'_y;n_y} = \frac{V_{\mathrm{B}}}{[2^{(n_y+n'_y)}\; n_y! n'_y!]^{\frac{1}{2}}} \frac{e^{-[(\beta_0^2 y_0^2)/(1+\beta_0^2 a_w^2)]}}{(1+\beta_0^2 a_w^2)^{\frac{1}{2}}} \sum_{k=0}^{min(n_y,n'_y)} 2^k\; k! \binom{n_y}{k} \binom{n'_y}{k}$$
$$\times \left(\frac{\beta_0^2 a_w^2}{(1+\beta_0^2 a_w^2)} \right)^{(\frac{n_y+n'_y}{2}-k)} \mathrm{H}_{n_y+n'_y-2k} \left(\frac{\beta_0 y_0}{(1+\beta_0^2 a_w^2)^{\frac{1}{2}}} \right). \tag{A.27}$$

Matrix elements of the coupling window potential

The potential V_{CW} plays the 'scattering' role in the central system. It allows interference between the two wires beyond the tunneling. The coupling window potential is

$$V_{\mathrm{CW}}(x,y) = -\sum_{i=1}^{j} V_{W_i}\, e^{(-\beta_{x_i}^2 (x-x_i)^2 - \beta_{y_i}^2 (y-y_i)^2)}, \tag{A.28}$$

If $j = 1$ there will be a single coupling window, but if $j = 2$ double coupling window exist in the barrier between the two wires. The matrix elements can be expressed as

$$(V_{\mathrm{CW}})_{n';n} = \langle n' | V_{\mathrm{CW}}(x,y) | n \rangle = -\sum_{i=1}^{j} V_{\mathrm{W}_i}\, V_{n'_x;n_x,i} V_{n'_y;n_y,i}. \tag{A.29}$$

$V_{n'_x,n_x} = \langle n'_x | e^{-\beta_x^2 x^2} | n_x \rangle$ and $V_{n'_y,n_y} = \langle n'_y | e^{-\beta_y^2 y^2} | n_y \rangle$. We first calculate $V_{n'_x,n_x}$, with the basis wave functions different for even and odd values of the quantum numbers (n_x, n'_x), so there are four possibilities to perform the integral in terms of the quantum numbers

- n_x is odd n'_x is odd
- n_x is odd n'_x is even
- n_x is even n'_x is odd
- n_x is even n'_x is even

If n_x and n'_x is odd integer, the matrix elements are

$$\begin{aligned} V_{n'_x,n_x} &= \langle n'_x | e^{-\beta_x^2 x^2} | n_x \rangle \\ &= \frac{2}{L_x} \int_{-\frac{L_x}{2}}^{+\frac{L_x}{2}} dx \cos\left(\frac{n'_x \pi x}{L_x}\right) e^{-\beta_x^2 (x-x_0)^2} \cos\left(\frac{n'_x \pi x}{L_x}\right), \end{aligned} \tag{A.30}$$

using $u_x = \dfrac{x}{L_x}$ we have

$$V_{n'_x,n_x} = 2 \int_{-\frac{1}{2}}^{+\frac{1}{2}} du_x \cos(n'_x \pi u_x)\, e^{-[\beta_x L_x (u_x - u_{x_0})]^2} \cos(n_x \pi u_x). \tag{A.31}$$

If n_x, n'_x are even integers we will have

$$V_{n'_x,n_x} = 2 \int_{-\frac{1}{2}}^{+\frac{1}{2}} du_x \sin(n'_x \pi u_x)\, e^{-[\beta_x L_x (u_x - u_{x_0})]^2} \sin(n_x \pi u_x). \tag{A.32}$$

Note that the integral will be zero for the other two cases. Rearranged the matrix elements are

$$V_{n'_x,n_x} = \begin{cases} 2 \int_{-\frac{1}{2}}^{+\frac{1}{2}} du_x \cos(n'_x \pi u_x)\, e^{-[\beta_x L_x (u_x - u_{x_0})]^2} \cos(n_x \pi u_x), & \text{if } n_x, n'_x = \text{odd}, \\ \\ 2 \int_{-\frac{1}{2}}^{+\frac{1}{2}} du_x \sin(n'_x \pi u_x)\, e^{-[\beta_x L_x (u_x - u_{x_0})]^2} \sin(n_x \pi u_x), & \text{if } n_x, n'_x = \text{even}. \end{cases} \tag{A.33}$$

We solve the Eq. (A.33) numerically.

The matrix elements of $V_{n'_y;n_y}$ are derived analytically and we already have done it for the middle barrier matrix elements. The same steps can be done to get $V_{n'_y,n_y}$, but we use β_y here instead of β_0 earlier

$$\begin{aligned} V_{n'_y;n_y} = {} & \frac{1}{[2^{(n_y+n'_y)}\, n_y! n'_y!]^{\frac{1}{2}}} \frac{e^{-[(\beta_y^2 y_0^2)/(1+\beta_y^2 a_w^2)]}}{(1+\beta_0^2 a_w^2)^{\frac{1}{2}}} \sum_{k=0}^{min(n_y,n'_y)} 2^k\, k! \binom{n_y}{k} \binom{n'_y}{k} \\ & \times \left(\frac{\beta_y^2 a_w^2}{(1+\beta_y^2 a_w^2)}\right)^{(\frac{n_y+n'_y}{2}-k)} \mathrm{H}_{n_y+n'_y-2k}\left(\frac{\beta_y y_0}{(1+\beta_y^2 a_w^2)^{\frac{1}{2}}}\right). \end{aligned} \tag{A.34}$$

Finally the coupling window potential gives

$$V_{n';n} = -\sum_{i=1}^{j} V_{\mathrm{W}_i}\, V_{n'_x;n_x,i} V_{n'_y;n_y,i}. \tag{A.35}$$

A.2 The Leads

Here, the theoretical framework of a lead Hamiltonian and it's matrix elements is introduced. Assuming the leads and the central system to have the same confinement potential. The Hamiltonian of a semi-infinite lead in an external perpendicular magnetic field can be described by

$$h_l = \frac{1}{2m^*}\left[p+e\mathbf{A}\right]^2 + W_{\mathrm{h}}^l(x) + W_{\mathrm{p}}^l(y), \tag{A.36}$$

the first term is the kinetic part, and the confining potentials $W_{\mathrm{h}}^l(x)$ and $W_{\mathrm{p}}^l(y)$ denote the hard wall and the parabolically confinement potential respectively, they have the following form

$$W_{\mathrm{h}}^{\mathrm{L}}(x) = \begin{cases} 0, & -\infty \geq x > -L_x/2, \\ \\ \infty, & \text{otherwise}, \end{cases} \qquad W_{\mathrm{h}}^{\mathrm{R}}(x) = \begin{cases} 0, & \infty \geq x > L_x/2, \\ \\ \infty, & \text{otherwise}, \end{cases} \tag{A.37}$$

and

$$W_{\mathrm{p}}^l(y) = \frac{1}{2}m^*\Omega_0^2 y^2. \tag{A.38}$$

Using these potentials one can write the Hamiltonian of a lead as

$$h_l = \frac{1}{2m^*}\left[p+e\mathbf{A}\right]^2 + \frac{1}{2}m^*\Omega_0^2 y^2, \tag{A.39}$$

if the magnetic field $\vec{B}$ to be in the z-direction, and the vector potential $\mathbf{A} = -By\hat{x}$. One can express the Hamiltonian as

$$h_l = \frac{1}{2m^*}\left[\frac{\hbar}{i}\nabla - eBy\vec{x}\right]^2 + \frac{1}{2}m^*\Omega_0^2 y^2, \tag{A.40}$$

rearranging the first term we obtain

$$h_l = -\frac{\hbar^2}{2m^*}\left(\Delta^2 - \frac{2i}{\ell^2}y\partial_x - \frac{y^2}{\ell^2}\right) + \frac{1}{2}m^*\Omega_0^2 y^2 \tag{A.41}$$

where the magnetic length $\ell = \sqrt{\hbar/eB}$. Rearranging the Hamiltonian again we get

$$h_l = \frac{p_{\mathrm{x}}^2}{2m^*} + \frac{p_{\mathrm{y}}^2}{2m^*} + \frac{1}{2}m^*\Omega_w^2 y^2 + \omega_c y p_x. \tag{A.42}$$

Inserting the Hamiltonian into the Schrödinger equation gives

$$\left(\frac{p_{\mathrm{x}}^2}{2m^*}+\frac{p_{\mathrm{y}}^2}{2m^*}+\frac{1}{2}m^*\Omega_w^2y^2+\omega_c y p_x\right)\psi_{\mathbf{q}}^l(x,y)=E_{\mathbf{q}}\psi_{\mathbf{q}}^l(x,y). \tag{A.43}$$

The boundary conditions of the wavefunctions are different for both leads. The left lead boundary condition are (a) $\psi_{\mathbf{q}}^{\mathrm{L}}(-\frac{L_x}{2},y)$=0 and (b) $\psi_{\mathbf{q}}^{\mathrm{L}}(x,y\to\pm\infty)$=0 for the left lead, and the right lead boundary condition are (a) $\psi_{\mathbf{q}}^{\mathrm{R}}(\frac{L_x}{2},y)$=0 and (b) $\psi_{\mathbf{q}}^{\mathrm{R}}(x,y\to\pm\infty)$=0. Using the boundary conditions, the wave functions can be expanded as

$$\psi_{\mathbf{q}}^l(x,y)=\int d\mathbf{p}\, C^{n_y,n_y'}(q,p)\varphi_p^l(x)\phi_{n_y'}^l(y), \tag{A.44}$$

where $\varphi_p^l(x)$ and $\phi_{n_y'}^l(y)$ are complete basis wave functions of a lead Eq. (2.13) and Eq. (2.14). In Dirac notation the states can be expressed as $|qn_y\rangle$. One obtains the matrix elements

$$\langle qn_y|h_l|q'n_y'\rangle=\left\langle qn_y\left|\left(\frac{p_{\mathrm{x}}^2}{2m^*}+\frac{p_{\mathrm{y}}^2}{2m^*}+\frac{1}{2}m^*\Omega_w^2y^2+\omega_c y p_x\right)\right|q'n_y'\right\rangle, \tag{A.45}$$

that we can divide into three parts yielding the following forms

$$\langle qn_y|\left(\frac{p_{\mathrm{x}}^2}{2m^*}\right)|q'n_y'\rangle=\frac{\hbar\Omega_{\mathrm{w}}}{2}(a_wq')^2\;\delta_{n_y,n_y'}\delta(q-q'), \tag{A.46}$$

$$\langle qn_y|\left(\frac{p_{\mathrm{y}}^2}{2m^*}+\frac{1}{2}m^*\Omega_w^2y^2\right)|q'n_y'\rangle=\hbar\Omega_{\mathrm{w}}\left(n_y'+\frac{1}{2}\right)\;\delta_{n_y,n_y'}\delta(q-q'), \tag{A.47}$$

$$\langle qn_y|\omega_c y p_x|q'n_y'\rangle=\hbar\omega_c\;a_w\;I_{q,q'}\left[\sqrt{\frac{n_y'}{2}}\delta_{n_y,n_y'-1}+\sqrt{\frac{n_y'+1}{2}}\delta_{n_y,n_y'+1}\right], \tag{A.48}$$

where

$$I_{q,q'}=-\left(\frac{iqq'}{2\pi}\right)\frac{\wp}{(q^2-q'^2)}.$$

Substituting Eq. (A.46) to Eq. (A.48) into Eq. (A.45) the matrix elements of a lead Hamiltonian are presented as

$$\langle qn_y|h_l|q'n_y'\rangle=\Upsilon_{q',n_y'}^0\;\delta_{n_y,n_y'}\delta(q-q')+\hbar\omega_c\;a_w\;I_{q,q'}\Upsilon_{n_y,n_y'}^B, \tag{A.49}$$

herein,

$$\Upsilon_{q',n_y'}^0=\hbar\Omega_{\mathrm{w}}\left[\frac{1}{2}\left(a_wq'\right)^2+\left(n_y'+\frac{1}{2}\right)\right],$$

and

$$\Upsilon^{B}_{n_y,n'_y} = \sqrt{\frac{n'_y}{2}}\,\delta_{n_y,n'_y-1} + \sqrt{\frac{n'_y+1}{2}}\,\delta_{n_y,n'_y+1}.$$

We use the basis eigenstates of a semiinfinite wire without a magnetic field to expand a new state $|pm_y)$

$$|pm_y) = \sum_{n'_y}\int_0^\infty dq' C^{n'_y,m_y}(q',p)\;|q'n'_y\rangle, \tag{A.50}$$

where $C^{n'_y,m_y}(q',p)$ is a complex constant. The Schrödinger equation of the new eigenstate is

$$h_l|pm_y) = E_{p,n_y}|pm_y). \tag{A.51}$$

Inserting Eq. (A.50) into the Schrödinger equation yields

$$\sum_{n'_y}\int_0^\infty dq'\;\langle qn_y|h_l|q'n'_y\rangle\;C^{n'_y,m_y}(q',p) = E_{p,m_y}\;C^{n_y,m_y}(q,p), \tag{A.52}$$

Substituting Eq. (A.49) into the above equation gives

$$\begin{aligned} E_{p,m_y}\;C^{n_y,m_y}(q,p) = &\sum_{n'_y}\int_0^\infty dq'\;\left[E^0_{q',n'_y}\;\delta_{n_y,n'_y}\delta(q-q')\right]C^{n'_y,m_y}(q',p) \\ &+\sum_{n'_y}\int_0^\infty dq'\left[\hbar\omega_c\;a_w\;I_{q,q'}E^B_{n_y,n'_y}\right]C^{n'_y,m_y}(q',p). \end{aligned} \tag{A.53}$$

Rearranging the terms, one explicity writes

$$\left[E_{p,m_y} - E^0_{q,n_y}\right]\;C^{n_y,m_y}(q,p) = \sum_{n'_y}\int_0^\infty dq'\left[\hbar\omega_c\;a_w\;I_{q,q'}E^B_{n_y,n'_y}\right]C^{n'_y,m_y}(q',p), \tag{A.54}$$

and inserting $I_{q,q'}$ into the above equation we get

$$\left[E_{p,m_y} - E^0_{q,n_y}\right]\;C^{n_y,m_y}(q,p) = \left(\frac{iq\;a_w\hbar\omega_c}{2\pi}\right)\sum_{n'_y}E^B_{n_y,n'_y}\int_0^\infty dq'\frac{q'\wp}{(q'^2-q^2)}\;C^{n'_y,m_y}(q',p). \tag{A.55}$$

Let's first take the integral part

$$\int_0^\infty dq'\frac{q'\wp}{(q'^2-q^2)}\;C^{n'_y,m_y}(q',p) = \frac{1}{2}\int_{-\infty}^\infty dq'\frac{q'\wp}{(q'^2-q^2)}\;C^{n'_y,m_y}(q',p),$$

using the Residual Theorem, one obtains

$$I_c = \frac{1}{2}\oint dq' \frac{q'}{(q'^2 - q^2)}\, C^{n'_y,m_y}(q',p) = \frac{1}{2}\, 2\pi i\, Res\left(\frac{q'}{(q'^2 - q^2)}\, C^{n'_y,m_y}(q',p), q\right), \tag{A.56}$$

and the Residue gives

$$\begin{aligned} Res\left(\frac{q'}{(q'^2 - q^2)}\, C^{n'_y,m_y}(q',p),\ q\right) &= \lim_{q' \to\, q} (q' - q) \frac{q' C^{n'_y,m_y}(q',p)}{(q'^2 - q^2)} \\ &= \frac{C^{n'_y,m_y}(q',p)}{2}. \end{aligned}$$

Inserting the value of Residue in the Eq. (A.56), we obtain

$$I_c = \pi i\, \frac{C^{n'_y,m_y}(q',p)}{2},$$

from the Fig. A.1 we can divide the integration into four parts

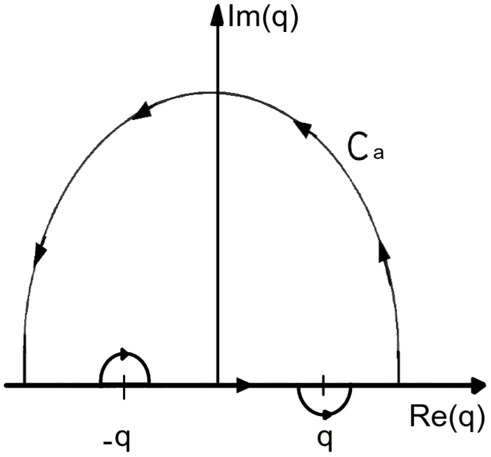

Figure A.1: Schematic of the contour integration in the complex plane.

$$I_c = \frac{1}{2}\int_{-\infty}^{\infty} dq' \frac{q' \wp}{(q'^2 - q^2)}\, C^{n'_y,m_y}(q',p) + \int_{c_a} .. + i\pi\, Res\, F(q) - i\pi\, Res\, F(-q), \tag{A.57}$$

$F(q)$ is the integrand. We can get the result for the integral of Eq. (A.55) as

$$\frac{1}{2}\int_{-\infty}^{\infty} dq' \frac{q' \wp}{(q'^2 - q^2)}\, C^{n'_y,m_y}(q',p) = \frac{i\pi}{2} C^{n'_y,m_y}(q,p). \tag{A.58}$$

Inserting Eq. (A.58) into Eq. (A.55) the final result is

$$\sum_{n'_y}\left[\delta_{n_y,n'_y}E^0_{q,n'_y}-\frac{\hbar\omega_c a_w}{4}\,q\,E^B_{n_y,n'_y}\right]C^{n'_y,m_y}(q,p)=E_{p,m_y}C^{n_y,m_y}(q,p). \tag{A.59}$$

A linear coupled system of algebraic eigenvalue equations that can be solved numerically. Evaluating the countour integral we assume that no bound states are formed in the semi-infinite quantum wire in the external magnetic field.

Appendix B

The many-electron eigenvalue problem

We start from the fundamental properties of Fermi creation and annihilation operators [37]

$$d^{\dagger}_{n'}d_{n}|i_{1}^{\nu},i_{2}^{\nu},\dots,i_{n}^{\nu},\dots,i_{N_{\mathrm{SES}}}^{\nu}\rangle = i_{n}^{\nu}\;|i_{1}^{\nu},i_{2}^{\nu},\dots,i_{n}^{\nu},\dots,i_{N_{\mathrm{SES}}}^{\nu}\rangle, \tag{B.1}$$

with

$$d_{n}|i_{1}^{\nu},i_{2}^{\nu},\dots,i_{n}^{\nu},\dots,i_{N_{\mathrm{SES}}}^{\nu}\rangle = \begin{cases} (-1)^{\alpha_{n}}|i_{1}^{\nu},i_{2}^{\nu},\dots,0,\dots,i_{N_{\mathrm{SES}}}^{\nu}\rangle & \text{if} \quad i_{n}^{\nu}=1, \\ 0 & \text{if} \quad i_{n}^{\nu}=0. \end{cases} \tag{B.2}$$

$$d_{n}^{\dagger}|i_{1}^{\nu},i_{2}^{\nu},\dots,i_{n}^{\nu},\dots,i_{N_{\mathrm{SES}}}^{\nu}\rangle = \begin{cases} 0 & \text{if} \quad i_{n}^{\nu}=1. \\ (-1)^{\alpha_{n}}|i_{1}^{\nu},i_{2}^{\nu},\dots,1,\dots,i_{N_{\mathrm{SES}}}^{\nu}\rangle & \text{if} \quad i_{n}^{\nu}=0, \end{cases} \tag{B.3}$$

here $\alpha_{n} = \sum_{j=1}^{n-1} i_{n}^{\nu}$.

The language of second quantization is used to describe the Hamiltonian of the system in the many-electron basis. In the second quantization, all operator can be expressed in terms of the fundamental creation and annihilation operators. The Hamiltonian of the isolated central system including the Coulomb interaction has the following form

$$H_{\mathrm{S}} = \sum_{n} E_{n} d_{n}^{\dagger} d_{n} + \frac{1}{2} \sum_{n',m'} \sum_{n,m} V_{n',m';n,m} d_{n'}^{\dagger} d_{m'}^{\dagger} d_{n} d_{m}, \tag{B.4}$$

E_n are the energy of the single electron states of the central sample. To calculate the interacting many-electron eigenvalues we define

$$\mathscr{E}^I_{\nu'\nu} = \langle \nu' | H_\mathrm{S} | \nu \rangle, \tag{B.5}$$

where $\mathscr{E}^I_{\nu'\nu}$ is a matrix element of the interacting many-electron Hamiltonian. Inserting Eq. (B.4) into Eq. (B.5) we obtain

$$\mathscr{E}^I_{\nu'\nu} = \sum_n E_n \, \langle \nu' | d_n^\dagger d_n | \nu \rangle + \frac{1}{2} \sum_{n',m'} \sum_{n,m} V_{n',m';n,m} \langle \nu' | d_{n'}^\dagger d_{m'}^\dagger d_n d_m | \nu \rangle, \tag{B.6}$$

the matrix elements of the Coulomb interacting in the single electron basis is given by

$$V_{n',m';n,m} = \langle n'm' | V | nm \rangle = \int d\mathbf{r} d\mathbf{r}' \, \psi^\mathrm{S}_{n'}(\mathbf{r})^* \psi^\mathrm{S}_{m'}(\mathbf{r}')^* V(\mathbf{r}-\mathbf{r}') \psi^\mathrm{S}_n(\mathbf{r}) \psi^\mathrm{S}_m(\mathbf{r}'), \tag{B.7}$$

with the Coulomb kernel given by

$$V(\mathbf{r}-\mathbf{r}') = \frac{e^2}{4\pi\varepsilon_0\varepsilon_r} \frac{1}{\sqrt{(x-x')^2+(y-y')^2+\eta^2}}. \tag{B.8}$$

Scaling in the natural energy and length scale here, one explicity writes

$$\frac{e^2}{4\pi\varepsilon_0\varepsilon_r} = \hbar\Omega_w \frac{a_w}{a_0^*}, \tag{B.9}$$

where a_0^* is effective Bohr radius which is 9.79 nm for GaAs semiconductor material. Substituting Eq. (B.8) into Eq. (B.7) we get

$$V_{n',m';n,m} = \int d\mathbf{r} \; \psi^\mathrm{S}_{n'}(\mathbf{r})^* \; I_{m',m} \; \psi^\mathrm{S}_n(\mathbf{r}), \tag{B.10}$$

with

$$I_{m',m} = \int d\mathbf{r}' \psi^\mathrm{S}_{m'}(\mathbf{r}')^* V(\mathbf{r}-\mathbf{r}') \psi^\mathrm{S}_m(\mathbf{r}'). \tag{B.11}$$

Now revisiting Eq. (B.6) and using the non-interacting MESs in Eq. (2.20), the first term can be written as

$$\mathscr{E}^0_{\nu'\nu} = \sum_n E_n i_n^\nu. \tag{B.12}$$

$\mathscr{E}^0_{\nu'\nu}$ is the non-interacting many-electron energy. Finally the matrix elements of the interacting many-electron Hamiltonian are

$$\mathscr{E}^I_{\nu'\nu} = \mathscr{E}^0_{\nu'\nu} + \frac{1}{2} \sum_{n',m'} \sum_{n,m} V_{n',m';n,m} \langle \nu' | d_{n'}^\dagger d_{m'}^\dagger d_n d_m | \nu \rangle. \tag{B.13}$$

The eigenvalue equation is solved numerically in a truncated many-electron basis.

Appendix C

The QGME Formalism

We start from the quantum Liouville-von Neumann (L-N) equation to derive the QGME

$$\frac{d\rho(t)}{dt} = -\frac{i}{\hbar}[H(t),\rho(t)] \equiv -i\mathscr{L}\,\rho(t), \tag{C.1}$$

$\rho(t)$ is the full density operator that describes the statistical state of the composite system, and the Liouville super-operator is $\mathscr{L} = \mathscr{L}_{\text{Sample}} + \mathscr{L}_{\text{Leads}} + \mathscr{L}_{\text{Transfer}}$. We use the Nakajima and Zwanzig formalism to project the full density operator into two parts

$$\rho(t) = \mathscr{P}\rho(t) + (1-\mathscr{P})\rho(t), \tag{C.2}$$

with $\mathscr{P} = \rho_l \text{Tr}_{\text{Leads}}$ being a super-operator. Substituting Eq. (C.2) into Eq. (C.1) and applying the projection operators $\mathscr{P}$ and Q to the L-N equation the following set of coupled differential equations is obtained

$$\mathscr{P}\frac{d\rho(t)}{dt} = -i\mathscr{P}\mathscr{L}\mathscr{P}\rho(t) - i\mathscr{P}\,\mathscr{L}\,Q\rho(t), \tag{C.3}$$

$$Q\frac{d\rho(t)}{dt} = -iQ\,\mathscr{L}\,\mathscr{P}\rho(t) - i\,Q\mathscr{L}\,Q\rho(t), \tag{C.4}$$

where $Q = (1-\mathscr{P})$. The first equation describes the time evolution of the relevant part while the second one describes the evolution of the irrelevant part of the system. Using the projection operator properties such as

- $\mathscr{P}\mathscr{L}\mathscr{P} = \mathscr{L}_{\text{Sample}}\mathscr{P}$,
- $\mathscr{P}\mathscr{L}Q = \mathscr{P}\mathscr{L}_{\text{Transfer}}Q$,

- $Q\mathscr{L}\mathscr{P} = Q\mathscr{L}_{\text{Transfer}}\mathscr{P}$,
- $Q\mathscr{L}Q = (\mathscr{L}_{\text{Sample}} + \mathscr{L}_{\text{Leads}} + Q\,\mathscr{L}_{\text{Transfer}})Q$.

The two coupled equations can be expressed as

$$\mathscr{P}\frac{d\rho(t)}{dt} = -i\mathscr{L}_{\text{Sample}}\mathscr{P}\rho(t) - i\mathscr{P}\,\mathscr{L}_{\text{Transfer}}\,Q\rho(t), \tag{C.5}$$

$$Q\frac{d\rho(t)}{dt} = -i\mathscr{L}_{\text{Transfer}}\,\mathscr{P}\rho(t) - i(\mathscr{L}_{\text{Sample}} + \mathscr{L}_{\text{Leads}} + Q\,\mathscr{L}_{\text{Transfer}})\,Q\rho(t). \tag{C.6}$$

A formal solution of the second equation is given by

$$Q\rho(t) = -i\int_{t_0}^{t} dt'\; Te^{-i\int_{t'}^{t''} dt''(\mathscr{L}_{\text{Sample}}+\mathscr{L}_{\text{Leads}}+Q\,\mathscr{L}_{\text{Transfer}})}\;\mathscr{L}_{\text{Transfer}}\mathscr{P}\rho(t'), \tag{C.7}$$

where the initial condition $QW(0) = 0$ is used, and T is a time ordering operator. Under the assumption of a weak-coupling $Q\mathscr{L}_{\text{Transfer}} = 0$, and denoting $\mathscr{L}_{\text{Transfer}}$ as $\mathscr{L}_{\text{T}}$ one obtains

$$Q\rho(t) = -i\int_{t_0}^{t} dt'\; Te^{-i\int_{t'}^{t''} dt''(\mathscr{L}_{\text{Sample}}+\mathscr{L}_{\text{Leads}})}\;\mathscr{L}_{\text{T}}\mathscr{P}\rho(t'), \tag{C.8}$$

if $\mathscr{L}_{\text{Sample}}$ and $\mathscr{L}_{\text{Leads}}$ are time-independent we obtain

$$Q\rho(t) = -i\int_{t_0}^{t} dt'\; e^{-i(\mathscr{L}_{\text{Sample}}+\mathscr{L}_{\text{Leads}})(t-t')}\;\mathscr{L}_{\text{T}}\mathscr{P}\rho(t'), \tag{C.9}$$

denoting $\mathscr{L}_0 = \mathscr{L}_{\text{Sample}} + \mathscr{L}_{\text{Leads}}$, Eq. (C.9) gives

$$Q\rho(t) = -i\int_{t_0}^{t} dt' e^{-\frac{i}{\hbar}H_0(t-t')}\;\mathscr{L}_{\text{T}}\mathscr{P}\rho(t')\; e^{\frac{i}{\hbar}H_0(t-t')}, \tag{C.10}$$

where $H_0 = H_{\text{Sample}} + H_{\text{Leads}}$. Substituting Eq. (C.10) into the second term of Eq. (C.5) with using $\mathscr{P} = \rho_l \text{Tr}_{\text{Leads}}$ we obtain

$$\mathscr{P}\frac{d\rho(t)}{dt} = -i\mathscr{L}_{\text{S}}\mathscr{P}\rho(t) - \rho_l \text{Tr}_{\text{Leads}}\left\{\mathscr{L}_{\text{T}}\int_{t_0}^{t} dt'\; U_0(t-t')\;\mathscr{L}_{\text{T}}\mathscr{P}\rho(t')\;U_0^{\dagger}(t-t')\right\}, \tag{C.11}$$

where $U_0(t-t') = e^{-\frac{i}{\hbar}H_0(t-t')}$ is the evolution operator of the closed system. Our system is weakly coupled, so higher than second order terms have been neglected in the expansion of the kernal of the equation. In that case the tunneling of the electrons is the so-called sequential tunneling.

The reduced density operator (RDO) of the central system can be defined as the trace of the full density operator of the composite system with respect to the reservoirs

$$\rho_{\mathrm{S}}(t) = \mathrm{Tr}_{\mathrm{Leads}}(\mathscr{P}\rho(t)). \tag{C.12}$$

In the weak coupling approximation the density matrix of the leads ρ_l is only negligible affected by the coupling. Using this approximation and taking one more trace ($\mathrm{Tr}_{\mathrm{Leads}}$) in the Eq. (C.11) to get

$$\frac{d\rho_{\mathrm{S}}(t)}{dt} = -i\mathscr{L}_{\mathrm{S}}\rho_{\mathrm{S}}(t) - \mathrm{Tr}_{\mathrm{Leads}}\left\{\mathscr{L}_{\mathrm{T}}\int_{t_0}^{t} dt'\; U_0(t-t')\; \mathscr{L}_{\mathrm{T}}\rho_l\rho_{\mathrm{S}}(t')\; U_0^{\dagger}(t-t')\right\}, \tag{C.13}$$

with $\mathrm{Tr}_{\mathrm{Leads}}\,\rho_l = 1$. From the Eq. (C.1) we can write $\mathscr{L}_{\mathrm{T}}\rho_l\rho_{\mathrm{S}}(t') = \frac{1}{\hbar}\left[H_{\mathrm{T}}^{l}(t'), \rho_l\rho_{\mathrm{S}}(t')\right]$, the Eq. (C.13) becomes

$$\begin{aligned}\frac{d\rho_{\mathrm{S}}(t)}{dt} &= -\frac{i}{\hbar}[H_{\mathrm{S}}, \rho_{\mathrm{S}}(t)] \\ &\quad -\frac{1}{\hbar^2}\mathrm{Tr}_{\mathrm{Leads}}\left\{\left[H_{\mathrm{T}}^{l}(t), \int_{t_0}^{t} dt' U_0(t-t')\;\left[H_{\mathrm{T}}^{l}(t'), \rho_l\rho_{\mathrm{S}}(t')\right]\; U_0^{\dagger}(t-t')\right]\right\}.\end{aligned} \tag{C.14}$$

It is clear that the density operator ρ_{S} is nonlocal in time, which gives us the non-Markovian approximation limit.

To simplify the expression one can rewrite the equation of motion for the RDO in the following form[38]

$$\frac{d\rho_{\mathrm{S}}(t)}{dt} = -i\mathscr{L}_{\mathrm{eff}}\rho_{\mathrm{S}}(t) + \int_{t_0}^{t} dt'\mathscr{K}(t,t')\rho_{\mathrm{S}}(t'), \tag{C.15}$$

where,

$$\mathscr{L}_{\mathrm{eff}}\rho_{\mathrm{S}}(t) = \frac{1}{\hbar}[H_{\mathrm{S}}, \rho_{\mathrm{S}}(t)], \tag{C.16}$$

and

$$\mathscr{K}(t,t')\rho_{\mathrm{S}}(t') = -\frac{1}{\hbar^2}\mathrm{Tr}_{\mathrm{Leads}}\left\{[H_{\mathrm{T}}^{l}(t), U_0(t-t')\;[H_{\mathrm{T}}^{l}(t'), \rho_l\rho_{\mathrm{S}}(t')]\; U_0^{\dagger}(t-t')]\right\}. \tag{C.17}$$

$\mathscr{L}_{\mathrm{eff}}$ stands for the effective Liouvillian and $\mathscr{K}(t,t')$ denotes the integration kernel [38].

By taking the second term of Eq. (C.15), one can perform the commutator relations getting the following form

$$\begin{aligned}\int_{t_0}^{t} dt'\mathscr{K}(t,t')\rho_{\mathrm{S}}(t') = -\frac{1}{\hbar^2}\mathrm{Tr}_l \int_{t_0}^{t} dt' \qquad\qquad (\mathrm{C}.18)\\ \times\{H_{\mathrm{T}}^l(t)U_0(t-t')H_{\mathrm{T}}^l(t')U_0^{\dagger}(t-t')U_0(t-t')\rho_{\mathrm{S}}(t')U_0^{\dagger}(t-t')\rho_l\\ -H_{\mathrm{T}}^l(t)U_0(t-t')\rho_{\mathrm{S}}(t')U_0^{\dagger}(t-t')\rho_l U_0(t-t')H_{\mathrm{T}}^l(t')U_0^{\dagger}(t-t')\\ -U_0(t-t')H_{\mathrm{T}}^l(t')U_0^{\dagger}(t-t')U_0(t-t')\rho_{\mathrm{S}}(t')U_0^{\dagger}(t-t')\rho_l H_{\mathrm{T}}^l(t)\\ +U_0(t-t')\rho_{\mathrm{S}}(t')U_0^{\dagger}(t-t')\rho_l U_0(t-t')H_{\mathrm{T}}^l(t')U_0^{\dagger}(t-t')H_{\mathrm{T}}^l(t)\}.\end{aligned}$$

As we mentioned the transfer Hamiltonians in the single-electron basis has the following form

$$H_{\mathrm{T}}^l(t) = \chi^l(t)\sum_n \int d\mathbf{q}\, \left[{c_{\mathbf{q}}^l}^{\dagger} T_{\mathbf{q}n}^l d_n + d_n^{\dagger}(T_{n\mathbf{q}}^l)^{\dagger} c_{\mathbf{q}}^l\right]. \qquad (\mathrm{C}.19)$$

We use the completeness of the MESs $\sum_\nu |\nu)(\nu| = \mathbf{1}$ to convert $H_{\mathrm{T}}^l(t)$ to the many-electron basis, we get

$$H_{\mathrm{T}}^l(t) = \chi^l(t)\int d\mathbf{q}\, \left(\mathscr{T}^l(\mathbf{q})c_{\mathbf{q}}^l + {c_{\mathbf{q}}^l}^{\dagger}(\mathscr{T}^l(\mathbf{q}))^{\dagger}\right), \qquad (\mathrm{C}.20)$$

where $\mathscr{T}^l(\mathbf{q})$ is the many-electron coupling matrix for non-interacting electrons

$$\mathscr{T}^l(\mathbf{q}) = \sum_{\nu,\nu'} \mathscr{T}_{\nu,\nu'}^l(\mathbf{q})\ |\nu')(\nu|, \qquad (\mathrm{C}.21)$$

with $\mathscr{T}_{\nu\nu'}^l(\mathbf{q}) = \sum_n T_{n\mathbf{q}}^l(\nu|d_n^{\dagger}|\nu')$ in terms of the single-electron coupling matrix $T_{n\mathbf{q}}^l$.

Substituting Eq. (C.20) into Eq. (C.18), and doing these steps; (a) using the property $[H_{\mathrm{Sample}}, H_{\mathrm{Lead}}] = 0$, the evolution operator can be separated into two parts $U_0(t-t') = U_{\mathrm{S}}(t-t')U_{\mathrm{L}}(t-t')$, (b) using the cyclicity of the trace with respect to $\mathrm{Tr}_{\mathrm{Lead}}$ and H_{Lead} the terms are reduced by $\mathrm{Tr}_l(\widetilde{c}_{\mathbf{q}}(t)\widetilde{c}_{\mathbf{q}}'(t)\rho_l) = 0$, where $\widetilde{c}_{\mathbf{q}}(t)$ is introduced in terms of the leads Hamiltonian as $\widetilde{c}_{\mathbf{q}}(t) = \exp(\frac{i}{\hbar}H_{\mathrm{Leads}}t)\times$

$c_{\mathbf{q}} \times \exp(-\frac{i}{\hbar} H_{\text{Leads}} t)$. Then Eq. (C.18) gives

$$
\begin{aligned}
\int_{t_0}^{t} dt' \mathscr{K}(t,t')\rho_{\text{S}}(t') = -\frac{\chi^l(t)}{\hbar^2} \int_{t_0}^{t} dt' \chi^l(t') \int d\mathbf{q} d\mathbf{q}' \qquad\qquad (\text{C.22})\\
\times [\, \mathscr{T}^l(\mathbf{q}) U_{\text{S}}(t-t') (\mathscr{T}^l(\mathbf{q}'))^\dagger \rho_{\text{S}}(t') U_{\text{S}}^\dagger(t-t') \,\text{Tr}_l(\widetilde{c}_{\mathbf{q}'}^\dagger(t')\widetilde{c}_{\mathbf{q}}(t)\rho_l)\\
+ (\mathscr{T}^l(\mathbf{q}'))^\dagger U_{\text{S}}(t-t') \mathscr{T}^l(\mathbf{q}) \rho_{\text{S}}(t') U_{\text{S}}^\dagger(t-t') \,\text{Tr}_l(\widetilde{c}_{\mathbf{q}'}(t')\widetilde{c}_{\mathbf{q}}^\dagger(t)\rho_l)\\
- U_{\text{S}}(t-t') (\mathscr{T}^l(\mathbf{q}'))^\dagger \rho_{\text{S}}(t') U_{\text{S}}^\dagger(t-t') \mathscr{T}^l(\mathbf{q}) \,\text{Tr}_l(\widetilde{c}_{\mathbf{q}}(t)\widetilde{c}_{\mathbf{q}'}^\dagger(t')\rho_l)\\
- U_{\text{S}}(t-t') \mathscr{T}^l(\mathbf{q}) \rho_{\text{S}}(t') U_{\text{S}}^\dagger(t-t') (\mathscr{T}^l(\mathbf{q}'))^\dagger \,\text{Tr}_l(\widetilde{c}_{\mathbf{q}}^\dagger(t)\widetilde{c}_{\mathbf{q}'}(t')\rho_l)\\
- \mathscr{T}^l(\mathbf{q}) U_{\text{S}}(t-t') \rho_{\text{S}}(t') (\mathscr{T}^l(\mathbf{q}'))^\dagger U_{\text{S}}^\dagger(t-t') \,\text{Tr}_l(\widetilde{c}_{\mathbf{q}'}^\dagger(t')\widetilde{c}_{\mathbf{q}}(t)\rho_l)\\
- (\mathscr{T}^l(\mathbf{q}'))^\dagger U_{\text{S}}(t-t') \rho_{\text{S}}(t') \mathscr{T}^l(\mathbf{q}) U_{\text{S}}^\dagger(t-t') \,\text{Tr}_l(\widetilde{c}_{\mathbf{q}'}(t')\widetilde{c}_{\mathbf{q}}^\dagger(t)\rho_l)\\
+ U_{\text{S}}(t-t') \rho_{\text{S}}(t') (\mathscr{T}^l(\mathbf{q}'))^\dagger U_{\text{S}}^\dagger(t-t') \mathscr{T}^l(\mathbf{q}) \,\text{Tr}_l(\widetilde{c}_{\mathbf{q}}(t)\widetilde{c}_{\mathbf{q}'}^\dagger(t')\rho_l)\\
+ U_{\text{S}}(t-t') \rho_{\text{S}}(t') \mathscr{T}^l(\mathbf{q}) U_{\text{S}}^\dagger(t-t') (\mathscr{T}^l(\mathbf{q}'))^\dagger \,\text{Tr}_l(\widetilde{c}_{\mathbf{q}}^\dagger(t)\widetilde{c}_{\mathbf{q}'}(t')\rho_l)\,].
\end{aligned}
$$

Using the identities

$$
\begin{aligned}
\text{Tr}_l\left(\widetilde{c}_{\mathbf{q}}(t)\widetilde{c}\dagger_{\mathbf{q}'}(t)\rho_l\right) &= e^{-i(t-t')\varepsilon^l(\mathbf{q})}\delta(\mathbf{q}-\mathbf{q}')\left(1-f(\varepsilon^l(\mathbf{q}))\right),\\
\text{Tr}_l\left(\widetilde{c}\dagger_{\mathbf{q}'}(t)\widetilde{c}_{\mathbf{q}}(t)\rho_l\right) &= e^{i(t-t')\varepsilon^l(\mathbf{q})}\delta(\mathbf{q}-\mathbf{q}')\left(f(\varepsilon^l(\mathbf{q}))\right),
\end{aligned}
\qquad (\text{C.23})
$$

and performing the Delta-integral $\int d\mathbf{q}'\delta(\mathbf{q}-\mathbf{q}')$, we obtain

$$
\begin{aligned}
\int_{t_0}^{t} dt' \mathscr{K}(t,t')\rho_{\text{S}}(t') = -\frac{\chi^l(t)}{\hbar^2} \int_{t_0}^{t} dt' \chi^l(t') \int d\mathbf{q}\\
\times [\, \mathscr{T}^l(\mathbf{q}) U_{\text{S}}(t-t') (\mathscr{T}^l(\mathbf{q}'))^\dagger \rho_{\text{S}}(t') U_{\text{S}}^\dagger(t-t') \,(1-f(\varepsilon^l(\mathbf{q})))e^{-i(t-t')\varepsilon^l(\mathbf{q})}\\
- \mathscr{T}^l(\mathbf{q}) U_{\text{S}}(t-t') \rho_{\text{S}}(t') (\mathscr{T}^l(\mathbf{q}'))^\dagger U_{\text{S}}^\dagger(t-t') \,f(\varepsilon^l(\mathbf{q}))e^{-i(t-t')\varepsilon^l(\mathbf{q})}\\
- U_{\text{S}}(t-t') (\mathscr{T}^l(\mathbf{q}'))^\dagger \rho_{\text{S}}(t') U_{\text{S}}^\dagger(t-t') \mathscr{T}^l(\mathbf{q}) \,(1-f(\varepsilon^l(\mathbf{q})))e^{-i(t-t')\varepsilon^l(\mathbf{q})}\\
+ U_{\text{S}}(t-t') \rho_{\text{S}}(t') (\mathscr{T}^l(\mathbf{q}'))^\dagger U_{\text{S}}^\dagger(t-t') \mathscr{T}^l(\mathbf{q}) \,f(\varepsilon^l(\mathbf{q}))e^{-i(t-t')\varepsilon^l(\mathbf{q})}\\
+ U_{\text{S}}(t-t') \rho_{\text{S}}(t') \mathscr{T}^l(\mathbf{q}) U_{\text{S}}^\dagger(t-t') (\mathscr{T}^l(\mathbf{q}'))^\dagger \,(1-f(\varepsilon^l(\mathbf{q})))e^{i(t-t')\varepsilon^l(\mathbf{q})}\\
- U_{\text{S}}(t-t') \mathscr{T}^l(\mathbf{q}) \rho_{\text{S}}(t') U_{\text{S}}^\dagger(t-t') (\mathscr{T}^l(\mathbf{q}'))^\dagger \,f(\varepsilon^l(\mathbf{q}))e^{i(t-t')\varepsilon^l(\mathbf{q})}\\
- (\mathscr{T}^l(\mathbf{q}'))^\dagger U_{\text{S}}(t-t') \rho_{\text{S}}(t') \mathscr{T}^l(\mathbf{q}) U_{\text{S}}^\dagger(t-t') \,(1-f(\varepsilon^l(\mathbf{q})))e^{i(t-t')\varepsilon^l(\mathbf{q})}\\
+ (\mathscr{T}^l(\mathbf{q}'))^\dagger U_{\text{S}}(t-t') \rho_{\text{S}}(t') \mathscr{T}^l(\mathbf{q}) U_{\text{S}}^\dagger(t-t') \,f(\varepsilon^l(\mathbf{q}))e^{i(t-t')\varepsilon^l(\mathbf{q})}\,].
\end{aligned}
\qquad (\text{C.24})
$$

Rearranging the terms

$$\begin{aligned}\int_{t_0}^{t} dt' \mathscr{K}(t,t')\rho_{\mathrm{S}}(t') = -\frac{\chi^l(t)}{\hbar^2}\int_{t_0}^{t} dt' \chi^l(t') \int d\mathbf{q} & \qquad (\mathrm{C.25})\\
\times [\, \mathscr{T}^l(\mathbf{q}')U_{\mathrm{S}}(t-t') \times \{(\mathscr{T}^l(\mathbf{q}'))^{\dagger}\rho_{\mathrm{S}}(t')(1-f(\varepsilon^l(\mathbf{q}))) - & \\
\rho_{\mathrm{S}}(t')(\mathscr{T}^l(\mathbf{q}'))^{\dagger} f(\varepsilon^l(\mathbf{q}))\} \times U_{\mathrm{S}}^{\dagger}(t-t')e^{-i(t-t')\varepsilon^l(\mathbf{q})} & \\
- U_{\mathrm{S}}(t-t') \times \{(\mathscr{T}^l(\mathbf{q}'))^{\dagger}\rho_{\mathrm{S}}(t')(1-f(\varepsilon^l(\mathbf{q}))) - & \\
\rho_{\mathrm{S}}(t')(\mathscr{T}^l(\mathbf{q}'))^{\dagger} f(\varepsilon^l(\mathbf{q}))\} \times U_{\mathrm{S}}^{\dagger}(t-t')\mathscr{T}^l(\mathbf{q})e^{-i(t-t')\varepsilon^l(\mathbf{q})} & \\
+ U_{\mathrm{S}}(t-t') \times \{\rho_{\mathrm{S}}(t')\mathscr{T}^l(\mathbf{q})(1-f(\varepsilon^l(\mathbf{q}))) - & \\
\mathscr{T}^l(\mathbf{q})\rho_{\mathrm{S}}(t') f(\varepsilon^l(\mathbf{q}))\} \times U_{\mathrm{S}}^{\dagger}(t-t')(\mathscr{T}^l(\mathbf{q}))^{\dagger} e^{i(t-t')\varepsilon^l(\mathbf{q})} & \\
- (\mathscr{T}^l(\mathbf{q}))^{\dagger} U_{\mathrm{S}}(t-t') \times \{\rho_{\mathrm{S}}(t')\mathscr{T}^l(\mathbf{q})(1-f(\varepsilon^l(\mathbf{q}))) - & \\
\mathscr{T}^l(\mathbf{q})\rho_{\mathrm{S}}(t') f(\varepsilon^l(\mathbf{q}))\} \times U_{\mathrm{S}}^{\dagger}(t-t')e^{i(t-t')\varepsilon^l(\mathbf{q})}\,], &\end{aligned}$$

and rewriting the evolution operator as $U_{\mathrm{S}}(t-t') = e^{-\frac{i}{\hbar}H_{\mathrm{Sample}}(t-t')} = e^{-\frac{i}{\hbar}H_{\mathrm{Sample}}t} * e^{\frac{i}{\hbar}H_{\mathrm{Sample}}t'}$, and denoting

$$\begin{aligned}\Omega^l(q) = e^{-\frac{i}{\hbar}H_{\mathrm{Sample}}t}\int_{t_0}^{t} dt'\, \chi^l(t') & \qquad (\mathrm{C.26})\\
\times e^{\frac{i}{\hbar}H_{\mathrm{Sample}}t'} \Big((\mathscr{T}^l(\mathbf{q}'))^{\dagger}\rho_{\mathrm{S}}(t')(1-f(\varepsilon^l(\mathbf{q}))) - \rho_{\mathrm{S}}(t')(\mathscr{T}^l(\mathbf{q}'))^{\dagger} f(\varepsilon^l(\mathbf{q}))\Big) & \\
\times e^{-\frac{i}{\hbar}H_{\mathrm{Sample}}t'} \times e^{\frac{i}{\hbar}H_{\mathrm{Sample}}t} e^{-i(t-t')\varepsilon^l(\mathbf{q})}. &\end{aligned}$$

Insertion of Eq. (C.26) into Eq. (C.25) yields

$$\begin{aligned}\int_{t_0}^{t} dt' \mathscr{K}(t,t')\rho_{\mathrm{S}}(t') = -\frac{\chi^l(t)}{\hbar^2}\int d\mathbf{q} \times \Big(\mathscr{T}^l(\mathbf{q})\Omega^l(\mathbf{q}) - \Omega^l(\mathbf{q})\mathscr{T}^l(\mathbf{q})\Big) &\\
-\frac{\chi^l(t)}{\hbar^2}\int d\mathbf{q}\Big((\Omega^l(\mathbf{q}))^{\dagger}(\mathscr{T}^l(\mathbf{q}))^{\dagger} - (\Omega^l(\mathbf{q}))^{\dagger}(\mathscr{T}^l(\mathbf{q}))^{\dagger}\Big). & \qquad (\mathrm{C.27})\end{aligned}$$

Finally we obtain the equation of motion for the RDO

$$\frac{d\rho_{\mathrm{S}}(t)}{dt} = -\frac{i}{\hbar}\left[H_{\mathrm{Sample}}, \rho_{\mathrm{S}}(t)\right] - \frac{1}{\hbar^2}\sum_{l=L,R}\chi^l(t)\int d\mathbf{q}\,\Big(\Big[\mathscr{T}^l(q), \Omega^l_{\mathbf{q}}(t)\Big] + \mathrm{h.c.}\Big), \qquad (\mathrm{C.28})$$

herein,

$$\Omega^l_{\mathbf{q}}(t) = U_{\mathrm{S}}^{\dagger}(t)\int_{t_0}^{t} dt'\, \chi^l(t')\Pi^l_{\mathbf{q}}(t') \times\, e^{\left(-\frac{i}{\hbar}(t-t')\varepsilon^l(\mathbf{q})\right)}U_{\mathrm{S}}(t),$$

with

$$\Pi_q^l(t') = U_{\mathrm{S}}(t') \left[\left(\mathscr{T}^l(\mathbf{q}) \right)^\dagger \rho_{\mathrm{S}}(t') \left(1 - f^l\left(\varepsilon(\mathbf{q})\right) \right) - \rho_{\mathrm{S}}(t') \left(\mathscr{T}^l(\mathbf{q}) \right)^\dagger f^l\left(\varepsilon(\mathbf{q})\right) \right] \times U_{\mathrm{S}}^\dagger(t').$$

$U_{\mathrm{S}}(t) = e^{iH_{\mathrm{S}}t/\hbar}$ denotes the time evolution operator and $f^l\left(\varepsilon(\mathbf{q})\right) = \{\exp[\varepsilon(\mathbf{q}) - \mu_l] + 1\}^{-1}$ indicates the Fermi function in the l lead at $t = t_0$.

Bibliography

[1] P. Johansson, *Resonant tunneling with a time-dependent voltage*, Phys. Rev. B **41**, 9892 (1990).

[2] L. Y. Chen and C.S. Ting, *Path-integral approach to transient transport of a double-barrier resonant-tunneling system*, Phys. Rev. B **41**, 8533 (1990).

[3] T. Kwapinski, R. Taranko, and E. Taranko, *Band structure effects in time-dependent electron transport through the quantum dot*, Phys. Rev. B **66**, 035315 (2002).

[4] T. Kwapinski, *Time-dependent electron transport through a quantum wire*, Phys. Rev. B **69**, 153303 (2004).

[5] S. Kurth, G. Stefanucci, C.-O. Almbladh, A. Rubio, and E. K. U. Gross, *Time-dependent quantum transport: A practical scheme using density functional theory*, Phys. Rev. B **72**, 035308 (2005).

[6] Joseph Maciejk, Jian Wang, and Hong Guo, *Time-dependent quantum transport far from equilibrium: An exact nonlinear response theory*, Phys. Rev. B **74**, 085324 (2006).

[7] Carsten Timm, *Tunneling through molecules and quantum dots: Master-equation approaches*, Phys. Rev. B **77**, 195416 (2008).

[8] J. König, J. Schmid, H. Schoeller, and G. Schön, *Resonant tunneling through ultrasmall quantum dots: Zero-bias anomalies, magnetic-field dependence, and boson-assisted transport*, Phys. Rev. B **54**, 16820 (1996).

[9] J. König, H. Schoeller, and G. Schön, *Cotunneling and renormalization effects for the single-electron transistor*, Phys. Rev. B **58**, 7882 (1998).

[10] F. Haake, *Density Operator and Multitime Correlation Functions for Open Systems*, Phys. Rev. A **3**, 1723 (1971).

[11] A. Braggio, J. König, and R. Fazio, *Full Counting Statistics in Strongly Interacting Systems: Non-Markovian Effects*, Phys. Rev. Lett., **96**, 026805 (2006).

[12] C. Emary, D. Marcos, R. Aguado, and T. Brandes, *Frequency-dependent counting statistics in interacting nanoscale conductors*, Phys. Rev. B **76**, 161404(R) (2007).

[13] A. Bednorz and W. Belzig, *Formulation of Time-Resolved Counting Statistics Based on a Positive-Operator-Valued Measure*, Phys. Rev. Lett. **101**, 206803 (2008).

[14] V. Gudmundsson, C. Gainar, C.-S. Tang, V. Moldoveanu, and A. Manolecu, *Time-dependent transport via the generalized master equation through a finite quantum wire with an embedded subsystem*, New J. Phys. **11**, 113007 (2009).

[15] E. Vaz and J. Kyriakidis, *Transient dynamics of confined charges in quantum dots in the sequential tunneling regime*, Phys. Rev. B **81**, 085315 (2010).

[16] J. Rammer, A. L. Shelankov, and J. Wabnig, *Quantum measurement in charge representation*, Phys. Rev. B **70**, 115327 (2004).

[17] J. Y. Luo, X.-Q. Li, and Y. J. Yan, *Calculation of the current noise spectrum in mesoscopic transport: A quantum master equation approach*, Phys. Rev. B **76**, 085325 (2007).

[18] S. Welack, M. Esposito, U. Harbola, and S. Mukamel, *Interference effects in the counting statistics of electron transfers through a double quantum dot*, Phys. Rev. B, **77**, 195315 (2008).

[19] C.-S. Tang, W, W. Yu, and V. Gudmundsson, *Tuning of coupling modes in laterally parallel double open quantum dots*, Phys. Rev. B **72**, 195331 (2005).

[20] V. Gudmundsson and C.-S. Tang, *Magnetotransport in a double quantum wire: Modeling using a scattering formalism built on the Lippmann-Schwinger equation*, Phys. Rev. B **74**, 125302 (2006).

[21] P. A. Orellana, F. Domínguez-Adameb, E. Diezc, *Dicke effect in a quantum wire with side-coupled quantum dots*, Physica E **35**, 126 (2006).

[22] O. Valsson, C.-S. Tang, and V. Gudmundsson, *Coherent switching by detuning a side-coupled quantum-dot system*, Phys. Rev. B **78**, 165318 (2008).

[23] R. Schuster *et al.*, Nature (London) **385**, 417 (1997).

[24] M. Avinun-Kalish *et al.*, Nature (London) **436**, 529 (2005).

[25] K.-W. Chen and C.-R. Chang, *Quantum interference and spin polarization on Rashba double quantum dots embedded in a ring*, Phys. Rev. B **78**, 235319 (2008).

[26] C. C. Eugster and J. A. del Alamo, *Tunneling spectroscopy of an electron waveguide*, Phys. Rev. Lett. **67**, 3586 (1991).

[27] D. M. Schroer, A. K. Huttel, K. Eberl, S. Ludwig, M. N. Kiselev, and B. L. Altshuler, *Kondo effect in a one-electron double quantum dot: Oscillations of the Kondo current in a weak magnetic field*, Phys. Rev. B **74**, 233301 (2006).

[28] V. Moldoveanu, A. Manolescu, and V. Gudmundsson, *Geometrical effects and signal delay in time-dependent transport at the nanoscale*, New J. Phys. **11**, 073019 (2009).

[29] Martin P A and Rothen F 2004 in *Many-Body Problem and Quantum Field Theory: An Introduction 2nd edn*, (Berlin, Springer).

[30] C. Yannouleas and U. Landman, *Symmetry breaking and quantum correlations in finite systems: studies of quantum dots and ultracold Bose gases and related nuclear and chemical methods*, Rep. Prog. Phys. **70**, 2067 (2007).

[31] Paul W. in *Festschrift zum 60. Geburstage A. Sommerfeld, S.30.Leipzig*, (Hirzel, 1928).

[32] Nakajima S., *On Quantum Theory of Transport Phenomena*, Progr. Theor. Phys. **20**, 948 (1958).

[33] Zwanzig R., *Ensemble method in the theory of irreversibility*, J. Chem. Phys. **33**, 1338 (1960).

[34] M. Esposito, U. Harbola, and S. Mukamel, *Nonequilibrium fluctuations, fluctuation theorems, and counting statistics in quantum systems*, Rev. Mod. Phys. **81**, 1665 (2009).

[35] Kenji Sasaoka, Takahiro Yamamoto, and Satoshi Watanabe, *Single-electron pumping from a quantum dot into an electrode*, Appl. Phys. Lett. **96**, 102105 (2010).

[36] Vidar Gudmundsson, Chi-Shung Tang, Olafur Jonasson, Valeriu Moldoveanu, and Andrei Manolescu, *Correlated time-dependent transport through a two-dimensional quantum structure*, Phys. Rev. B **81**, 205319 (2010).

[37] H. Bruus and K. Flensberg, in *Many-Body Quantum Theory in Condensed Matter Physics, An Introduction* (Oxford University Press, 2004).

[38] F. Haake, in *Quantum Statistics in Optics and Solid-state Physics*, edited by G. Hohler and E.A. Niekisch, Springer Tracts in Modern Physics Vol. 66 (Springer, Berlin, Heidelberg, New York, 1973), p. 98.